1 **Diagnosing uncertainties in global biomass burning emission inventories and**

2 **their impact on modeled air pollutants**

3 Wenxuan Hua[1,2,] Sijia Lou[1,2,3*], Xin Huang[1,2,3], Lian Xue[1,2,3], Ke Ding[1,2,3] Zilin Wang[1,2],

4 Aijun Ding[1,2,3]

5 [1] Joint International Research Laboratory of Atmospheric and Earth System Sciences,

6 School of Atmospheric Sciences, Nanjing University, Nanjing 210023, China.

7 [2] Jiangsu Provincial Collaborative Innovation Center for Climate Change, Nanjing,

8 China.

9 [3] Frontiers Science Center for Critical Earth Material Cycling, Nanjing University,

10 Nanjing, China.

11

12 Corresponding author: Sijia Lou (lousijia@nju.edu.cn)

13

14 Abstract

15 Biomass burning (BB) emission inventories are often used to understand the interactions of aerosols
16 with weather and climate. However, large uncertainties exist among current BB inventories, so the
17 choice of inventories can greatly affect model results. To quantify the differences among BB
18 emission inventories and reveal their reasons, we compared carbon monoxide (CO) and organic
19 carbon (OC) emissions from seven major BB regions globally from 2013 to 2016. The current
20 inventories are based on two basic approaches: (1) bottom-up approach, which establishes
21 inventories based on observed surface data, and (2) top-down approach, which based on the release
22 rate of radiative energy from vegetation burning. In this study, we selected mainstream bottom-up
23 inventories Fire INventory from NCAR 1.5 (FINN1.5) and Global Fire Emissions Database version
24 4s (GFED4s), and the top-down inventories Quick Fire Emissions Dataset 2.5 (QFED2.5) and
25 VIIRS-based Fire Emission Inventory version 0 (VFEI0). We find that the total global CO emissions
26 fluctuate between 252 and 336 Tg and the regional bias is even larger, which can be up to six times.
27 Dry matter is responsible for most of the regional variation in CO emissions (50-80%), with
28 emission factors accounting for the remaining 20-50%. Uncertainties in dry matter often come from
29 biases in the calculation of bottom fuel consumption and burned area, which are closely related to
30 vegetation classification methods and fire detection products. In the tropics, peatlands contribute
31 more fuel loads and higher emission factors than grasslands. At high latitudes, as cloud fraction
32 increases, the bias between burned area (or fire radiative power) increases by 20%. In addition, due
33 to the corrected emission factors in QFED2.5, global BB OC emissions have higher variability,
34 fluctuating between 14.9 and 42.9 Tg.
35 Finally, we applied the four sets of BB emission inventories to the Community Atmosphere Model
36 version 6 (CAM6) and compared the model results with observations. Our results suggest that the
37 simulations based on the GFED4s agree best with the MOPITT-retrieved CO. We also compared
38 the simulation results with satellite or ground-based measurments, such as Moderate Resolution
39 Imaging Spectroradiometer (MODIS) AOD and AErosol RObotic NETwork (AERONET) AOD.
40 Our results reveal that there is no global optimal choice for the BB inventories, but we give certain
41 inventory recommendations based on different study areas and spatiotemporal scales. This study
42 has implications for reducing the uncertainties in emissions or improving BB emission inventories
43 in further studies.

44

45

46 1 Introduction

47   In recent years, extreme wildfire events have occurred frequently around the world (Balshi et al.,
48 2009; Knorr et al., 2016; Yang et al., 2019; Junghenn Noyes et al., 2022). The size of the fire has
49 consistently broken records over the last decades (Westerling et al., 2006; Westerling and Bryant,
50 2008; Brando et al., 2020), threatened lives and infrastructure, and continuously jeopardized the
51 global economy. Wildfires are also one of the most important sources of biomass burning (BB)
52 emissions, which can emit loads of gaseous and particulate pollutants (Ferek et al., 1998; Adams et
53 al., 2019), detrimental to regional air quality and human health (Reid et al., 2005, Reid and Mooney,
54 2016). Additionally, BB aerosols, predominantly black carbon (BC) and organic carbon (OC) can
55 affect regional climate by absorbing/scattering solar radiation, acting as cloud condensation nuclei,
56 and altering cloud albedo (Spracklen et al., 2011; Boucher et al. 2013).

57   Recent studies have shown that aerosols produced by biomass burning can significantly affect
58   changes in temperature, cloud fraction, precipitation, and even the circulation structure (Christian
59   et al., 2019; Yang et al., 2019; Yu et al., 2019; Carter et al., 2020; Jiang et al.,2020; Ding et al.,
60   2021; Huang et al., 2023). Jiang et al. (2020) used the Community Earth System Model version 1.2
61   (CESM1.2) to investigate the impact of BB aerosols on global climate change. They pointed out
62   that BB aerosols reduce the annual mean surface air temperature and precipitation by 0.64 K and
63   0.06 mm day^{-1}, respectively. Based on 16 years of simulation from the Weather Research and
64   Forecasting model coupled with Chemistry (WRF-Chem), Ding et al. (2021) reported that BB
65   aerosols increased low cloud coverage by 20% in areas downwind of wildfires in Southeast Asia in
66   March and Southern Africa in August. A recent study also reported that the radiative effects of BB
67   aerosols alter the local circulation structure, leading to dry air on the West Coast of the United States,
68   or less precipitation in Southeast Asia, thus intensifying fires and exacerbating air pollution (Huang
69   et al., 2023). However, these simulated results are sensitive to the amount of BB pollutants (Liu et
70   al., 2020a).

71   Previous studies often found that there is a significant deviation between the gaseous or
72   particulate pollutants simulated by the model and the satellite retrieval value (Bian et al., 2007;
73   Chen et al., 2009; Carter et al., 2020), one of the most important reasons comes from the
74   uncertainties in emission inventories. For example, Bian et al. (2007) applied six different BB
75   emission inventories, GFED1 and GFED2 (Global Fire Emissions Database version 1 and 2)
76   (GFED1 and GFED2), Arellano1, Arellano2, Duncan1, and Duncan2, to the Unified Chemistry
77   Transport Model (UCTM). They reported that although the total global CO of the six BB emission
78   inventories was within 30% of each other, the model results suggested that regional deviations can
79   be much higher, by as much as 2-5 times, especially in the Southern Hemisphere. Bias in emission
80   inventories can therefore often have a significant impact on the direct and indirect effects of models
81   on aerosol assessments (Liu et al., 2018; Ramnarine et al., 2019; Carter et al., 2020). Carter et al.
82   (2020) compared the simulated black carbon (BC) and organic carbon (OC) concentrations with
83   measurements from IMPROVE (Interagency Monitoring of Protected Visual Environments)
84   observation network from May to September. They suggested that using the FINN1.5 inventory
85   (Fire INventory from NCAR 1.5) improves model results in eastern North America, while using
86   GFED4s, QFED2.4 (Quick Fire Emissions Dataset 2.4), and GFAS1.2 (Global Fire Assimilation
87   System 1.2) inventories shows better agreement with observations in western North America. They
88   also noted that population-weighted BB PM$_{2.5}$ concentrations in Canada and the adjacent United
89   States could vary between 0.5 and 1.6 μg m^{-3} in 2012 by using different BB emissions. Liu et al.
90   (2018) used the global model CAM5 (The Community Atmosphere Model 5) and three different
91   BB emission inventories to analyze the uncertainties in the aerosol radiative effects in the
92   Northeastern United States in early April 2009. They found that aerosols exhibited a stronger
93   cooling effect when CAM5 used the QFED2.4 inventory than the GFED3.1 and GFED4s
94   inventories, with additional cooling of -0.7 W m^{-2} and -1.2 W m^{-2} through aerosol direct radiative
95   effect and the aerosol-cloud radiative effect, respectively. On a global basis, Ramnarine et al. (2019)
96   used the global model GEOS-Chem-TOMAS (GEOS-Chem-TwO-Moment Aerosol Sectional), and
97   found that the direct radiative effects and indirect effects of aerosols driven by the FINN1.5 emission
98   inventory in 2010 were 70% and 10% lower than those driven by GFED4, respectively. Therefore,
99   to better estimate regional aerosol-radiation/aerosol-cloud interactions in wildfire regions, it is

100   necessary to understand the differences in emission inventories from biomass combustion and the
101   main drivers of uncertainties.

102   In general, BB emission inventories are based on bottom-up or top-down method to infer the
103   emission source intensity. The bottom-up approach, also known as the fire detection and/or burned
104   area method, estimates emissions based on surface data such as fuel loading, active fire counts,
105   and/or burned area. Currently, the widely used BB inventories based on bottom-up approach include
106   Duncan (Duncan, 2003), GFED (van der Werf et al., 2006, 2010a, 2010b, 2017), FINN
107   (Wiedingmyer et al., 2011), Global Inventory for Chemistry-Climate Studies-GFED4S (G-G)
108   (Mieville et al., 2010). The top-down approach uses satellite observations of fire radiative power
109   (FPR), a method to measure the radiative energy release rate of burning vegetation, to estimate
110   emissions by fuel consumption. The BB inventories based on top-down method include Arellano
111   (Arellano Jr et al., 2004; Arellano Jr and Hess, 2006), GFAS (Kaiser et al., 2012), Fire Energetics
112   and Emission Research (FEER) (Ichoku and Ellison, 2014), QFED (Darmenov et al., 2015), the
113   Fire Emissions Estimate Via Aerosol Optical Depth (FEEV-AOD) (Paton-Walsh et al., 2012) and
114   the recently released VIIRS-based Fire Emission Inventory version 0 (VFEI0) (Ferrada et al., 2022).
115   On a global scale, the average annual BB emissions of CO and OC can differ by a factor of 3 to 4,
116   with the global emissions fluctuating in the range of 280-580 Tg yr^{-1} and 13-50 Tg yr^{-1} respectively.
117   The bias may be even greater when focusing on emissions in specific regions (Bian et al., 2007;
118   Liousse et al., 2010; Williams et al., 2012; Carter et al., 2020; Lin et al., 2020b; Liu et al., 2020b).
119   For example, the estimated CO emission of Arellano inventory in South America during the burning
120   peak season of September 2000 is four times greater than that of GFED1 inventory (Bian et al.,
121   2007). A recent study even found that since 2008, OC emissions from QFED2.5 in the Middle East
122   are approximately 50 times larger than those from GFED3 and GFED4 (Pan et al., 2020).

123   Several previous studies have analyzed the reason for the huge emission bias. According to
124   Darmenov et al. (2015), the emissions E_i (mass of pollutant i) is the sum of the products of the
125   emission factor (EF_b) and the dry matter (DM_b) for each biome:

126
$$E_i = \sum_b EF_b \times DM_b \qquad (1)$$

127   While earlier studies suggested that the uncertainty in BB emissions arises mainly from differences
128   in emission factors (e.g., Alvarado et al., 2010; Akagi et al., 2011; Urbanski et al., 2011), more
129   recent studies point out that uncertainty in dry matter also plays an important role in differences in
130   BB emissions (Paton-Walsh et al., 2010; 2012; Carter et al., 2020). For example, Paton-Walsh et al.
131   (2012) assessed the difference in CO emissions from the February 2009 Australian fire and found
132   that total CO emissions in GFED3.1 were roughly three times higher than that in FINN1, with DM
133   contributing up to 80%. Carter et al. (2020) evaluated emissions from various North American BB
134   inventories over the period 2004-2016 and found that changes in DM was very close to emission
135   trend, suggesting that uncertainty in potential DM across the North American was the primary factor,
136   rather than EF.

137   To analyze the root causes of the differences in EFs and DM among BB inventories, equation (1)
138   is further decomposed. According to the bottom-up method, the emission for each species i can be
139   further summarized as:

140
$$E_i = \sum_b (EF_b \times BA(x,t) \times FC_b) = \sum_b (EF_b \times BA(x,t) \times FL_b \times FB_b) \qquad (2)$$

141   where BA(x,t) is burned area at location x and time t, which can be obtained from the fire detection
142   products. For each biome, fuel consumption (FC_b) is the product of fuel loadings (FL_b) and the
143   fraction of biomass burned (FB_b), which can be obtained with reference to static biomass density or

144   using a biological models.

145   Similarly, the top-down inventories can be further divided into:

146
$$E_i = \sum_b EF_b \times \alpha_b \times \frac{FRP}{A} \tag{3}$$

147   where A is the area of unit pixel observed by satellite, and FRP/A represents the FRP density, which

148   is proportional to E_i. For the emission E_i of a substance i, the empirical coefficient α_b is used to

149   convert the fire radiative energy (i.e., the time-integrated FRP) of each biome into DM (also can be

150   considered as converting FRP density into emission fluxes).

151   Therefore, land cover and land use (LULC) data associated with vegetation types can influence

152   the BB inventory by affecting EFs, fuel loads, and the FB for bottom-up approach, or by affecting

153   EFs and empirical coefficient α for top-down approach (Wiedinmyer et al., 2006; Ferrada et al.,

154   2022). For example, Wiedinmyer et al. (2006) used three different LULC products to drive a

155   regional model of BB emissions and found that varying LULC products drive through discrepancies

156   in fuel consumption, ultimately leading to an annual bias of up to 26% in North and Central America.

157   Furthermore, since EFs are highly dependent on various biomes, different biome classifications will

158   introduce uncertainty to BB emission inventories (Ferrada et al., 2022). In addition to LULC

159   products, fire detection products (such as FRP and burned area products) that are affected by satellite

160   transit time and cloud obscuration also bring uncertainty to BB emission inventories. For example,

161   Paton-Walsh et al. (2012) found that in an Australian fire called "Black Friday" in February 2009,

162   the burned areas of FINN1 were barely half of that of GFED3.1. Liu et al. (2020b) reported that

163   compared with the active fire area used in FINN1.5, the burned area product selected by GFED4s

164   is less sensitive to the satellite overpass time and cloud obscuration.

165   Although previous work has generated biomass burning emission inventories and attempted to

166   reduce their uncertainties (Duncan, 2003; Arellano Jr et al., 2004; Arellano Jr and Hess, 2006; van

167   der Werf et al., 2006, 2010a, 2010b, 2017; Bian et al., 2007; Mieville et al., 2010; Wiedingmyer et

168   al., 2011; Kaiser et al., 2012; Paton-Walsh et al., 2012; Ichoku and Ellison, 2014; Darmenov et al.,

169   2015; Liu et al., 2018; Ramnarine et al., 2019; Carter et al., 2020; Lin et al., 2020b; Liu et al., 2020b;

170   Pan et al., 2020; Zhang et al., 2020; Ferrada et al., 2022), they did not analyze the reasons why DM

171   and EF exhibited large differences among various emission inventories, which may vary over time

172   and location. Here, this study aims to explore the underlying reasons for the differences in BB

173   emission inventories in major combustion regions around the world, thereby attempting to reduce

174   the uncertainties of the impact of BB emission inventories on model results. To minimize the

175   interference of anthropogenic emissions on model results, we selected combustion regions

176   satisfying the following conditions: (1) regional BB CO emissions above 20 Tg yr^{-1}; (2) BB CO

177   emissions contribute more than 70% of the total. We ultimately selected seven major burning areas

178   as shown in Fig. 1, including Boreal North America (BONA), Southern Hemispheric South America

179   (SHSA), Northern Hemispheric Africa (NHAF), Southern Hemispheric Africa (SHAF), Boreal Asia

180   (BOAS), Southeast Asia and India (SEAS), and Equatorial Asia (EQAS).

181   Due to the abundance of published BB inventories, in this study we selected several datasets that

182   are widely used (FINN1.5, GFED4s, and QFED2.5) and the latest released VFEI0 for comparison,

183   with the former two of them based on bottom-up method and the others based on top-down method.

184   Specific details of BB inventories will be described in Section 2. In section 3.1, we will discuss the

185   differences of CO and OC emissions among four inventories, along with the contribution of DM

186   and EFs to the differences, respectively. For the first time, we have evaluated the biases of CO

187   column concentrations and AOD driven by BB inventories in the CESM2-CAM6 model, and given
188   suggestions on what inventory should be adopted across various regions (Section 3.2). The
189   conclusion and discussion are presented in section 4, and our research is anticipated to provide some
190   insights for reducing the uncertainties of BB emission datasets.
191
192   **2 Data and Methodology**

193   **2.1 Biomass Burning emission inventories**

194   We simultaneously diagnosed the differences among two bottom-up approach inventories and
195   two top-down approach inventories, including FINN1.5, GFED4s, and QFED2.5, which are
196   commonly used in the current atmospheric model, as well as the recently released VFEI0. Details
197   about the emission inventories and the satellite products they use are listed in Table 1.
198

199   **Bottom-up (Burned Area) inventories**

200   Among the four BB emission inventories selected in this study, FINN1.5 and GFED4s both use
201   the bottom-up method, also known as the Burned Area method. As shown in Table 1, FINN1.5 uses
202   the MODIS (Moderate Resolution Imaging Spectroradiometer) product MCD14DL to calculate the
203   burned area, which can monitor fire points with an area larger than 0.05 km^2. Since the MCD14DL
204   is an active fire detection product that reflects real-time fire point detection, if a fire occurs but the
205   satellite is not in transit or is obscured by clouds while the satellite is in transit, the fire will not be
206   detected (Firms, 2017). Additionally, considering that MODIS on polar-orbiting satellites cannot
207   provide daily coverage products in the tropics (30°N-30°S), FINN1.5 makes some smoothing
208   assumptions for fire detection in this region. It assumes that every fire detected at the equator will
209   continue the next day at half the size of the previous day (Table 1), and this assumption obviously
210   raises some questions (Wiedinmyer et al., 2011; Pan et al., 2020). Meanwhile, the classification of
211   land cover types in FINN1.5 is based on MCD12Q1 (IGBP, version 2005). According to the IGBP
212   land cover classification, each fire is initially assigned to one of 16 land use/land cover (LULC)
213   classes, and then lumped into six generic categories including tropical forest, temperate forest,
214   boreal forest, savanna and grasslands, woody savannas and shrublands, and cropland (Fig. S1,
215   Wiedingmyer et al., 2011). The amount of usable biomass that can be burned per fire (fuel loadings)
216   for each generic LULC according to Hoelzemann et al. (2004). The FB for each fire is specified as
217   a function of vegetation cover (MODIS Vegetation Continuous Fields (VCF) product), as described
218   by Wiedinmyer et al. (2006; 2011). Emission factors (EFs) for various gaseous and particulate
219   species are determined from a dataset compiled by Akagi et al. (2011) and Andreae and Merlet
220   (2001), and these EFs vary for different LULC types. Currently, FINN1.5 provides the daily global
221   emissions from biomass burning since 2002, including 41 species, with a spatial resolution of 1 km^2
222   (Table 1).
223   The main difference between FINN1.5 and GFED4s is that the latter mainly uses MCD64A1
224   Collection 5.1 burned area product (Giglio et al., 2013; Randerson et al., 2018), which can only
225   detect fires with a size larger than 500 m × 500 m. For small fire burning areas, GFED4s additionally
226   incorporate active fire detection products (MOD14A1 and MYD14A1), and by comparing the
227   difference normalized burned area (dNBR) of active fire products observed inside and outside the
228   500 m burning area, which compensates to some extent for the bias caused by the lower spatial
229   resolution of the original product MCD64A1 (van der Werf et al., 2017). Note that, according to van

230   der Werf et al. (2017), only small or moderate angel fire point detections are retained in order to
231   reduce uncertainty in geolocation. In general, burned area products reduce uncertainty in fire
232   detection due to satellite non-transit and cloud/smoke obscuration when burn occurs by identifying
233   day-to-day surface variations, such as charcoal and ash deposition, vegetation migration and
234   changes in vegetation structure (Boschetti et al., 2019). According to the annual MODIS MCD12C1
235   version 5.1 land cover type product and University of Maryland (UMD) classification scheme
236   (Friedl et al., 2010), each fire is also initially assigned to one of 16 LULC subcategories and then
237   lumped into six categories: tropical forest, temperate forest, boreal forest, savanna, cropland
238   (agriculture), and peatland as shown in Fig. S1. While GFED4s combines the "savanna and
239   grasslands" and "woody savannas and shrublands" in FINN1.5 into one biome, it has an additional
240   biome "peatland". GFED4s generate the fuel loadings and the fraction of biomass burned for each
241   category by combining the burned area and vegetation morality in a modified Carnegie-Ames-
242   Stanford Approach (CASA) model, which is driven by the data of temperature, precipitation, solar
243   radiation, NDVI, and vegetation types (Schaefer et al., 2008; van der Werf et al., 2010; 2017).
244   Additionally, EFs for various gaseous and particulate species follow Akagi et al. (2011) and Andreae
245   and Merlet (2001), also vary with different biome categories. Currently, GFED4s provides the daily
246   global emissions from biomass burning since 1997, including 27 species, with a spatial resolution
247   of $0.25° \times 0.25°$ (Table 1). However, since 2017, the DM provided by GFED4s is derived from a
248   linear relationship between past emissions and MODIS FRP data for the period 2003-2016.

249

Top-down (Fire Radiative Power) inventories

251   The other two emission inventories selected for this study, QFED2.5 and VFEI0, use a top-down
252   approach, also known as the Fire Radiative Power (FRP) method. Unlike the bottom-up approach,
253   the top-down approach is not based on fire point detection, but on satellite products that detected
254   fire radiated power. QFED2.5 use MODIS Collection 6 MOD14/MYD14 level 2 products to
255   estimate the fire radiative power, and use MOD03/MYD03 to pinpoint the location of the fire
256   (Darmenov and Silva 2015; Liu et al., 2020b). Since MOD14 and MYD14 products are strongly
257   influenced by clouds, missing FRPs are corrected using the "sequential approach" combining
258   current observations and predicted values (Darmenov and da Silva, 2015). The FRPs are then
259   integrated in time to obtain the fire radiative energy (FRE), which is detected and converted to DM
260   by an empirical coefficient α. The initial value of α in QFED2.5 is taken from Kaiser et al. (2009)
261   and subsequently adjusted monthly based on global emissions of GFED2 in 2003–2007, resulting
262   in two sets of empirical coefficients: $\alpha_{MOD14} = 1.89 \times 10^{-6}$ kg (DM) J^{-1} and $\alpha_{MYD14} = 0.644 \times 10^{-6}$ kg
263   (DM) J^{-1}. In QFED2.5, the International Geosphere-Biosphere Programme (IGBP-INPE) dataset
264   classes are used to aggregate 17 land cover classes to four broad vegetation types, including tropical
265   forest, extra-tropical forest (forest classes that exclude tropical forest), savanna, and grassland (Fig.
266   S1, Darmenov and da Silva 2015). The EFs of particulate or trace gas species are from previous
267   studies (Andreae and Merlet, 2001; Akagi et al., 2011). It is important to note that QFED2.5 scales
268   up the EFs for emissions associated with the particulate phase, such as organic carbon (OC), black
269   carbon (BC), ammonia (NH$_3$), sulfur dioxide (SO$_2$), and particulate matter diameter $< 2.5 \mu m$ (PM$_{2.5}$),
270   so emissions of these species are greater in QFED2.5 than in other inventories. The QFED2.5
271   product covers daily emission inventories from 2000 to the present, and contains 17 emission
272   species with a spatial resolution of up to $0.1° \times 0.1°$.

273   VFEI0 also adopts the top-down method but uses VNP14IMG.001 FRP product from VIIRS I-
274   band (Visible Infrared Imaging Radiometer), which can detect smaller and colder flames than
275   MODIS (1 km resolution at nadir), since it has a resolution of 375 m at nadir (Ferrada et al., 2022).
276   Unlike QFED2.5, VFEI0 has no cloud calibration, but it will be supplemented in future versions. It
277   also uses the empirical coefficient α to convert the detected FRE into DM, but α is derived from the
278   linear regression of GFED3.1DM and VIIRS FRP. Additionally, MCD12C1 (IGBP, version 2015)
279   is the underlying LULC data, which is further supplemented by Köppen climate classification (Beck
280   et al., 2018) to define ten subcategories in VFEI0 (i.e., Tropical forest, Savanna, Temperate forest,
281   Temperate Savanna, Boreal forest, Boreal Savanna, Grass, Agriculture, Peatland and Desertic areas).
282   VFEI0 then grouped the previous ten subcategories into six biomes (Fig. S1), corresponding to the
283   emission factors provided by Andreae (2019), to calculate the BB emission inventory. Among the
284   four BB emission inventories, VFEI0 provides the shortest inventory time coverage (daily emission
285   fluxes from 20 January 2012 to the present), but it provides the largest number of emitted species at
286   46 and the highest horizontal resolution of 0.005° × 0.005° (Table 1).

287

288   **2.2 Quantitative statistical methods**

289   As described in section 2.1, fire detection is greatly affected by cloud/smoke obscuration in the
290   bottom-up approach. For example, if there are clouds/smoke at high altitudes while fire occurs on
291   the ground, the MCD14DL active fire detection product used in FINN1.5 may miss these fire points.
292   In addition, for the combustion that is too small in size and too low in temperature, it cannot be
293   effectively monitored due to the low brightness temperature contrast with the surrounding
294   environment. In contrast, the burned area product (mainly MCD64A1) used by GFED4s determines
295   the burning information based on the changes such as surface albedo, and is therefore less affected
296   by clouds/smoke. For inventories based on the top-down approach, the emission inventories also
297   differ to a large extent due to the cloud/smoke obscuration, since QFED2.5 uses a "sequential
298   method" to correct for missing FRPs during cloud/smoke obscuration, whereas VFEI0 does not.
299   Thus, in this study, the symmetrical mean absolute percentage error (SMAPE) and Pearson's R are
300   used to access the difference in sensitivity to clouds/smoke between the two BB products based on
301   the bottom-up (or top-down) approach. The specific algorithm is as follows:

$$302 \quad \text{SMAPE} = \frac{100\%}{n} \sum_{i=1}^{n} \frac{|X-Y|}{(|X|+|Y|)/2}, \quad (4)$$

$$303 \quad R = \frac{\sum_{i=1}^{N} |(X-\bar{X}) \cdot (Y-\bar{Y})|}{\sqrt{\sum_{i=1}^{N}(X-\bar{X})^2 \cdot \sum_{i=1}^{N}(Y-\bar{Y})^2}}, \quad (5)$$

304   where X and Y are fire detection data from two different datasets (e.g. burned area from FINN1.5
305   and GFED4s or FRP from VFEI0 and QFED2.5). We divided these fire detection data into three
306   groups according to the cloud fractions less than 0.4, 0.4-0.7, and greater than 0.7, and the number
307   n represents valid samples in different cloud fraction groups. SMAPE ranges from 0% to 200%,
308   with smaller values indicating smaller differences, while Pearson's R ranges from 0 to 1, with
309   smaller values implying less correlation.
310   In order to quantify the effect of cloud obscuration on BB datasets, we selected the most intensely
311   burning regions in BONA in July for this study. For consistency, we re-interpolated the fire
312   detection data used in the four BB datasets, as well as the MODIS MCD06 cloud fraction data, to
313   the same horizontal resolution (0.25° × 0.25°). Considering the continuity of combustion, we took

314 every 5° × 5° as a sample area in the northern U.S. to ensure that if a large burn occurred, the area
315 would be detected to some extent, avoiding errors due to differences between the inventories. At
316 the same time, we excluded the samples in the same time and location, where the emissions are all
317 zero. Finally, a total of 1888 samples were obtained for the burned area group, with 534, 541, and
318 813 samples for low (<0.4), medium (0.4-0.7), and high (>0.7) cloud fraction, respectively. A total
319 of 1,682 samples were obtained for the FRP group, with 860, 390, and 432 samples under low,
320 medium, and high cloud fraction, respectively. It is worth noting that we use the average FRP of
321 MOD and MYD for QFED2.5 since the VFEI0 FRP is the average between day and nighttime
322 observations. Moreover, our approach cannot rule out the case of missing measurements when two
323 sets of BB inventories are both obscured by the cloud. However, the main goal of this paper is to
324 explore the causes of uncertainties in emission inventories, the specific case of omission due to
325 cloud obscuration depends on the development of satellite detection technology and is not part of
326 the purpose of this study.
327

2.3 CESM2-CAM6 model

329 The Community Earth System Model version 2.1 (CESM2) is a new generation of the coupled
330 climate/Earth system models developed by National Center for Atmospheric Research (NCAR). In
331 this study, we used the global Community Atmosphere Model version 6 (CAM6) (Danabasoglu et
332 al., 2020). Gas-phase chemistry was represented by the Model for Ozone and Related chemical
333 Tracers tropospheric chemistry (MOZART-T1, Emmons et al., 2020). The wet deposition of soluble
334 gaseous compounds in CAM6-Chem is based on the scheme of Neu and Prather (2012), which
335 describes the process of in-cloud cleaning and under-cloud cleaning. The formation of secondary
336 organic aerosols (SOA) is from a volatility basis set (VBS) approach developed by Tilmes (2019).
337 Properties and processes of aerosol species of black carbon (BC), primary organic aerosols (POA),
338 SOA, sulfate, dust, and sea salt are calculated by Modal Aerosol Module (MAM4) described by Liu
339 (2016). CAM6 uses a horizontal resolution of nominal 1° (1.25° × 0.9° , longitude by latitude) and
340 32 vertical levels from the surface to 2.26 hPa (~40 km).
341 In this study, four BB emission inventories (FINN1.5, GFED4s, QFED2.5 and VFEI0) are
342 regridded to a horizontal resolution of 1.25° (longitude) × 0.9° (latitude), and then applied to the
343 model. All simulations were performed for five years, while horizontal winds and temperature are
344 nudged toward the Modern-Era Retrospective analysis for Research and Applications, version 2
345 (MERRA-2) reanalysis data (GMAO, 2015) for every 6 h. Simulations are conducted for 2012-
346 2016, with the first year used for initialization and model spin-up. Daily BB emissions were applied
347 in this study, whereas the vertical distribution of fire emissions was followed Freitas et al. (2006,
348 2010). Anthropogenic and biogenic emissions in this study are from the Community Emissions Data
349 System (CEDS) and Model of Emissions of Gases and Aerosols from Nature version 2.1
350 (MEGANv2.1), respectively, at 2010 levels (Guenther et al.,2012; Hoesly et al., 2018).
351

2.4 Measurement data

353 The Tropospheric Pollution Measurement Instrument (MOPITT) is aboard the Earth Observing
354 System (EOS)/Terra satellite launched by NASA (Warner, et al., 2001). MOPITT is the first
355 instrument to observe the global concentration and currently provides column concentration and
356 volume mixing ratio of global carbon monoxide (CO) since 1999. We used MOPITT CO gridded

357 monthly means (Near and Thermal Infrared Radiances) V009 (MOP03JM_9; NASA Langley
358 Atmospheric Science Data Center DAAC, retrieved from
359 https://doi.org/10.5067/TERRA/MOPITT/MOP03JM.009), which has a horizontal resolution of 1°
360 × 1°. It should be noted that in order to compare the CO column concentration simulated by CESM2-
361 CAM6 with MOPITT CO, we calculated the simulated CO column concentrations by cumulative
362 integration from 900 hPa to 100 hPa isobaric height (Deeter et al., 2022). We also used the daily
363 AOD (550 nm) and cloud fraction data from MODIS products MOD08_D3 (MODIS/Terra Aerosol
364 Cloud Water Vapor Ozone Daily L3; Platnick et al. 2015) and MCD06COSP (MODIS (Aqua/Terra)
365 Cloud Properties Level 3 daily, Webb et al., 2017), respectively.

366 The observations of AERONET (http://AERONET.gsfc.nasa.gov/; Holben et al., 1998) from 12
367 sites are used in this study. These AERONET stations were selected since they are close to BB
368 source regions. As marked in Figure 1b, these sites include sites in BONA (Yellowknife_Aurora
369 (62.5°N, 114.4°W), Pickle Lake (51.4°N, 90.2°W)), BOAS (Tiksi (71.6°N, 128.9°E), Yakutsk
370 (61.7°N, 129.4°E)), SHAF (Namibe (15.2°S, 12.2°E), Mongu Inn (15.3°S, 23.1°E)), SHSA (Alta
371 Floresta (9.9°S, 56.1°W), Rio Branco (9.9°S, 67.9°W)), EQAS (Palangkaraya (2.2°S, 113.9°E),
372 Jambi (1.6°S, 103.6°E)), SEAS (Omkoi (17.8°N, 98.4°E), Ubon Ratchathani (15.2°N, 104.9°E)).

373 All observed AOD represent real atmospheric conditions and therefore, in addition to BB aerosols,
374 biogenic aerosols, anthropogenic aerosols, dust, and sea salts are also integrated in MODIS and
375 AERONET datasets.
376

3 Comparative analysis of emission inventories

378 CO and OC are the main species emitted from biomass burning (Westerling et al., 2010; van der
379 Werf et al., 2010b; Carter et al., 2020) but emissions vary widely. In this study, we compare the
380 differences in CO and OC emissions (representing gaseous and particulate pollutant, respectively)
381 in four BB inventories, and investigate in detail the key reasons for the differences in emission
382 inventories.

**3.1 The contribution of dry matter and emission factors to the difference in CO
emission**

385 The total global CO emissions from the four BB emission inventories selected for this study are
386 in the range of 252-336 Tg, with GFED4s being the highest and FINN1.5 the lowest. In order to
387 quantify the differences in CO emissions among four datasets, we use the standard deviation (SD)
388 to characterize the absolute difference, and the coefficient of variation (cv, calculate as the ratio of
389 SD to the mean) to characterize the relative differences (Fig. 2a). The larger the cv, the greater the
390 difference between emission inventories. We have ranked the major seven BB regions in the world
391 according to the differences in CO emissions between the four sets of inventories, with the
392 differences being, in descending order, EQAS, BONA, SEAS, SHAF, NHAF, BOAS, and SHSA.

393 This study points to a high variability of different BB emission inventories in EQAS, which is
394 inconsistent with previous studies (Liu et al., 2020b; Pan et al., 2020). Previous studies mainly
395 focused on emission differences of particulate pollutants, such as BC and OC (Bian et al., 2007;
396 Paton-Walsh et al., 2012; Carter et al., 2020; Lin et al., 2020b; Pan et al., 2020), thus assuming that
397 the inventory differences in Equatorial Asia are smaller than those in Southern Hemispheric Africa
398 and Northern Hemispheric Africa. In contrast, this study analyzes the differences between
399 particulate and gaseous pollutant emissions separately when comparing the differences in BB

400 emission inventories. For example, GFED4s classify a large portion of EQAS land cover as peatland
401 (Kasischke and Bruhwiler, 2002; Stockwell et al., 2016; van der Werf et al., 2006, 2010a, 2010b,
402 2017) and suggest that this organic matter-rich soil emits a large amount of CO when burned. The
403 other three inventories either do not include peatland (FINN1.5 and QFED2.5) or only consider
404 peatlands as a small fraction of the burned area in EQAS (VFEI0), thus estimating CO emissions
405 much smaller than GFED4s. In addition, the extent of peatland fires in EQAS increased significantly
406 during the strong El Niño event (Page et al., 2002). Considering that a strong El Niño event also
407 occurred in 2015-2016, these increases in peatland fires further amplify the discrepancy between
408 GFED4s and other emission inventories on CO estimates.
409   According to Eq. (1), we split the difference in CO emission into the difference in EFs and DM
410 (Fig. 2b and c). Since only GFED4s provides DM information in its dataset, we follow Carter (2020)
411 to divide CO emissions per grid by the EF applied to each biome to obtain DM:

$$DM_{b,x} = CO_{b,x}/EF_b \qquad (6)$$

413 where b represents one of the seven biomes in Fig. S1, and x represents the location grid. The
414 calculation of DM by CO is somewhat representative, since all inventories are not corrected for CO
415 emission factors. After calculating the $DM_{b,x}$ for each grid, we obtained a regional average emission
416 factor by dividing the total CO emissions by the total DM for each major BB region:

$$EF_{CO} = \sum_{b,x} CO / \sum_{b,x} DM \qquad (7)$$

418 Such calculations allow us to distinguish the impact of LULC classification on BB emission
419 inventories.
420   As shown in Fig. 2, the distribution pattern of DM differences is very similar to that of CO
421 emission differences, indicating that DM is the main reason for dominating the difference in the
422 four emission inventories. In comparison, the difference in DM contributes 50-80% to the regional
423 CO emission differences, and the comprehensive EFs contributes the remaining 20-50%. However,
424 in EQAS, BONA, and BOAS, the contribution of comprehensive EFs to BB emission differences
425 in four datasets is comparable to that of DM (Fig. 2). In the following sections, we will further
426 analyze the main causes of the differences for DM and EFs.

427 **3.2 Primary causes of DM inconsistency in the bottom-up inventories**

428   To investigate the underlying causes of the differences in DM, we first compared DM between
429 emission inventories produced by the bottom-up and up-down approaches. The difference in DM
430 estimated by the top-down method is small, and the DM ratio of QFED2.5 to VFEI0 does not exceed
431 two times in different regions. However, DM estimated by the bottom-up approach varied widely,
432 with DM ratio as high as 4.7 in BONA for GFED4s and FINN1.5 during 2013-2016 fire season.
433 Therefore, we need to focus on the main reasons for DM variance in emission inventories based on
434 bottom-up approach.
435   According to Eq. (2), DM equals the product of burned area, fuel load, and FB in the bottom-up
436 inventories, with the product of the last two terms being fuel consumption. Fig. 3 compares the
437 burned area and fuel consumption of GFED4s and FINN1.5 emission inventories for the seven
438 largest BB regions. The ratio GFED4s/FINN1.5 represents the relative difference in burned area or
439 fuel consumption between the two emission inventories. In general, the difference in burned area
440 between the two inventories varies greatly with latitude, and the ratio of GFED4s to FINN1.5
441 fluctuates in the range of 0.28-1.94. In contrast, differences in fuel consumption between the two
442 inventories were more consistent, with GFED4s consistently having higher fuel consumption than

443 FINN1.5 in all regions except SEAS. In the next sections, we discuss the main reasons for the
444 differences in burned area and fuel consumption between the two datasets.

3.2.1 Effect of land cover on burned area

446 As shown in Fig. 3a, the differences in burned area between the bottom-up emission inventories
447 is highly variable. At high latitudes, the burned area of GFED4s is significantly higher than that of
448 FINN1.5, especially in BONA, where the burned area of GFED4s is twice that of FINN1.5. In
449 contrast, the burned area of GFED4s in the equatorial region is much lower than that of FINN1.5,
450 and even 60% smaller in EQAS. This is a result of the difference in fire detection between the two
451 datasets. As shown in Table 1, FINN1.5 uses the MCD14 DL fire point product, while GFED4s uses
452 the hybrid burned area product, mainly using MCD64A1 combined with fire point products
453 MOD14A1/MYD14A1 to enhance the detection of small fires.
454 These two sets of products have their own advantages in detection ability under different
455 vegetation type conditions. The hybrid burned area product detects burned area over a period of
456 time (up to days), while fire point product detects burned area primarily in near real time (Roy et
457 al., 2008). In addition, the burned area used in GFED4s (hybrid burned area product) is not affected
458 by the vegetation canopy when the leaf area index (LAI) is less than 5. Therefore, higher burned
459 area is estimated in GFED4s in BONA and BOAS than in FINN1.5. However, in areas with more
460 broadleaf forests and grasslands such as EQAS, SEAS, and SHSA (Fig. S2), the MCD14DL fire
461 point product used in FINN1.5 performed better in capturing understory fires that occurred in closed
462 canopies (Cochrane and Laurance, 2002; Cochrane, 2003; Alencar et al., 2005; Roy et al., 2008). It
463 also has an advantage in capturing sporadic and fragmented small fires in grasslands and agricultural
464 fields due to its high resolution (Liu et al., 2020b). Furthermore, FINN1.5 assumes that each
465 detected fire in the equatorial region will continue to burn for 2 days, and that the next day's fire
466 will continue to be half the size of the previous day (Table 1). Thus, the burned area of FINN1.5 in
467 the tropical zone is 2.6 times higher than those of GFED4s, which is consistent with previous studies
468 (Wiedinmyer et al., 2011; Pan et al., 2020). At the equator, the burned area in grassland/agricultural
469 fields and forest estimated by FINN1.5 is 1-3 and 4-6 times higher than in GFED4s, respectively
470 (not shown).
471 It is worth noting that in Africa (NHAF and SHAF), although the dominant burnable vegetation
472 is grassland (Fig. S2), unlike the sporadic small fires that occur in grassland in the other five regions,
473 large continuous fires often occur in African Savannas (Liu et al., 2020b). Therefore, the hybrid
474 burned area product used in GFED4s is more effective in detecting all fire events occurring over a
475 period of time, with 10-20% higher burned area than FINN1.5.

3.2.2 Effect of cloud obscuration on burned area

477 In addition to the vegetation, cloud occlusion can likewise bias the satellite detection of burned
478 area. Figure S3 shows the time series of AOD measured by satellite or ground-based data at the
479 Pickle Lack site of BONA from June to August 2013. In contrast to the high AOD values observed
480 for the AERONET network, MODIS AOD is often in missing measurements when the MODIS
481 cloud fraction is larger than 0.5. Furthermore, AERONET AOD varies dramatically over a short
482 period of time, suggesting that different detection principles (such as detecting fire points in near
483 real-time during satellite overpass time, or estimating the accumulation of burned area over time

484   through changes in surface albedo over multiple satellite overpass times) can significantly affect the
485   burned area product under high cloud fraction/smoke conditions (Paton-Walsh et al., 2012; Liu et
486   al., 2020b; Pan et al., 2020). Although some assumptions are made in FINN1.5 in the equatorial
487   regions as described above to improve the effect of cloud obscuration on burned area detection,
488   these assumptions are not used for mid- and high-latitudes. GFED4s uses a hybrid burned area
489   product and is relatively unaffected by cloud obscuration. By fusing the MCD64A1 with
490   MOD14A1/MYD14A1 products with multi-temporal satellite data, GFED4s is able to determine
491   the approximate date and extent of fires through post-fire ash deposition, vegetation migration, and
492   land surface changes (van der Werf et al., 2017; Boschetti et al., 2015, 2019).

493   To quantitatively assess the impact of cloud obscuration on different emission inventory estimates,
494   we perform analyzes in areas with high cloud fraction (Fig. S4), intense biomass burning, and
495   unaffected by the smoothing hypothesis used in FINN1.5. We selected the regions of North America
496   with the most intense biomass burning (Alberta and Saskatchewan, Canada, 50°-70°E, 100°-130°W,
497   Fig. S5), and analyzed the relationship between the burned area and cloud fraction for bottom-up
498   inventories during July from 2013 to 2016 (Fig. S6). As shown in Fig. 4, with the increase in cloud
499   fraction, SMAPE of the two bottom-up emission inventories increases from 150% to 180%, while
500   the Pearson correlation declines from 0.85 to around 0.75. These results demonstrate that the
501   uncertainty in the burned area for two bottom-up emission inventories increases by ~20% during
502   high cloud fraction compared to low cloud fraction conditions.

3.2.3 Causes of Fuel Consumption differences

504   Fuel consumption is another factor that affects DM differences between two BB emission
505   inventories. As shown in Fig. 3b, the fuel consumption of GFED4s is 30-75% higher than that of
506   FINN1.5 in almost all BB areas except SEAS. The difference in fuel consumption between the two
507   emission inventories is larger in the tropics than in the high latitudes. In this study, we invert the
508   fuel consumption for each vegetation biome b in a given area as follows:

509    $$FC_b = DM_b/BA \qquad (8)$$

510   The DM corresponding to each biome in FINN1.5 and GFED4s has been obtained according to
511   equation (6), and BA is the total burned area obtained from the emission inventory. As shown in Fig.
512   5, at high latitudes (e.g., BONA and BOAS), and in the equatorial region (such as EQAS), relatively
513   high fuel consumption comes from peatlands in GFED4s. According to previous studies, peatlands,
514   a type of soil rich in organic matter, store large amounts of carbon underground (van der Werf et al.,
515   2010b, 2017; Gibson et al., 2018; Kiely et al., 2021; Vetrita et al., 2021), and emit large amounts of
516   CO when burned. Peatlands contribute 30-60% of the total fuel consumption in BONA, BOAS, and
517   EQAS (Fig. 5a-c).

518   Besides peatlands, GFED4s tends to have higher fuel consumption than FINN1.5 due to forest
519   contributions. Forests (including tropical, temperate, and boreal forests) account for more than 50%
520   of the fuel consumption in all burning regions except EQAS, where peatlands dominate the fuel
521   consumption. Moreover, forest fuel consumption in GFED4s is generally much higher than in
522   FINN1.5 except in BOAS and SEAS (Fig. 5). Since fuel consumption is equal to the product of fuel
523   load and FB (the percentage of specific plants that can be adequately burned, Eq. 2), different
524   vegetation classifications may be responsible for large differences in fuel consumption between
525   emission inventories. For example, for woody vegetation such as forests, GFED4s assumes a range
526   of FB between 40-60% for temperate and tropical forests and 20-40% for boreal forests, while

527 FINN1.5 assumes that all woody vegetation burns no more than 30% (van der Werf et al., 2010;
528 Wiedinmyer et al., 2011). Thus, in terms of FB alone, the forest fuel consumption of GFED4s is
529 therefore 0.67-1.3 times greater than that of FINN1.5, which is one of the main reasons for the
530 difference in fuel consumption.

531 **3.3 Primary causes of DM inconsistency in the top-down approach**

532 We also analyze the causes of the difference in DM between BB emission inventories estimated
533 by the top-down method. According to Eq. (3), it is evident that the empirical factor and the radiative
534 energy of the fire are the key factors that cause the discrepancy in the top-down emission inventories.
535 The QFED2.5 and VFEI0 inventories we have chosen use different satellites for the fire detection
536 products. For example, for the fire radiative power product, QFED2.5 is based on the Moderate
537 Resolution Imaging Spectroradiometer (MODIS) inversion of the NASA Terra and Aqua combined
538 satellites, while VFEI0 is based on the Visible Infrared Imaging Radiometer (VIIRS) inversion of
539 the combined polar orbiting satellites Suomi NPP and NOAA-20, although the algorithms are
540 similar. However, there are systematic deviations due to different satellites, specific tests and
541 metadata, and resolutions. The VIIRS 375 m fire product used by VFEI0 has a finer resolution and
542 is more advantageous for small fire spot detection than other coarser resolution (1 km) fire spot
543 detection products. The FRP density used in VFEI0 is much higher than that of QFED2.5 due to the
544 fine horizontal resolution.
545 The estimations of FRP and DM are highly dependent on the horizontal resolution of satellite
546 products. For example, in BONA in July (the month with the most intense burning at the position
547 of 50°-70°N, 100°-130°W) the total QFED FRP (average FRP measured by MOD and MYD) is 1.5
548 times higher than VFEI0 (Fig. S7), but DM in QFED2.5 inventory is 30% lower than VFEI0. The
549 high FRP density used in VFEI0 (Fig. S8) results in a higher DM than QFED2.5 due to its higher
550 horizontal resolution which facilitates capturing precise areas of fire. Note that the empirical factor
551 also has an impact on the amount of DM, but it should not be as significant as the difference caused
552 by the horizontal resolution of satellite products (Kaiser et al., 2012; Darmenov et al., 2015; Ferrada
553 et al. 2022).
554 Previous studies have shown that cloud occlusion also causes bias in FRP detection (Liu et al.,
555 2020b). We also take BONA as a pilot region to analyze the influence of cloud fraction on FRP in
556 QFED2.5 and VFEI0. According to Fig. 5c-d, the SMAPE of the two emission inventories rises as
557 the cloud fraction increases, and Pearson correlation is noticeably low under the maximum cloud
558 fraction. While QFED2.5 uses the "sequential approach" (section 2.1) to correct for the missing
559 FRP in cloud-obscured fires, this correction is not considered in VFEI0. Therefore, although the two
560 top-down emission inventories use similar algorithms, significant bias occurs under high cloud
561 fraction conditions, with QFED2.5 estimating DM much higher than VFEI0.

562 **3.4 Primary causes of EF inconsistencies**

563 Although DM differences dominate the inconsistencies of CO emissions across major BB regions,
564 the contribution of EFs is still not negligible in some regions. For example, in EQAS, BONA, and
565 BOAS, the contribution of EFs is up to 50%, which is comparable to that of DM. Considering that
566 EF is closely related to vegetation types, we calculated the emission factor of a single biome type
567 in a given region as follows:

$$EF_b = CO_b / \sum_b DM \qquad\qquad (8)$$

568

569 where b represents one of the seven biome classifications in this study (Fig. S1), and DM here is

570 the sum of the value from each biome in a certain region.

571   The comprehensive EFs of GFED4s are higher in BONA, BOAS, and EQAS regions than in

572 other inventories, with vegetation classification being one of the most important factors (Fig. 6).

573 For example, in EQAS at low latitudes, peatlands in GFED4s account for 65% of the regional

574 comprehensive EF. In contrast to GFED4s, FINN1.5, and QFED2.5 do not consider this organic

575 matter-rich land as a source of burning, and they classify this category of land cover type as savanna

576 or grass. The CO emission factor for peatlands is four times higher than the CO emission factor for

577 savanna or grass (Table 2), ultimately making the comprehensive EF for GFED4s 60-70% higher

578 than that of the other three datasets. It is worth noting that although the classification of Peatland

579 exists in VFEI0 (Ferrada et al., 2022), due to differences in terrestrial ecological divisions (Olson et

580 al., 2001; http://www.worldwildlife.org/science/data/item1875.html), peatlands identification areas

581 are much smaller than GFED4s inventory. Therefore CO emissions from peatlands in GFED4s are

582 much higher than in the VFEI0 inventory (Figure 3-9a; Ferrada et al., 2022).

583   In both BONA and BOAS, we find that the comprehensive EFs in the four datasets are ranked as

584 follows: GFED4s>FINN1.5>QFED2.5>VFEI0, where the EF of GFED4s is about 1.5 times higher

585 than that of VFEI0. Unlike the low-latitude regions, the classification of forests in different emission

586 inventories is the main reason for the difference in comprehensive EF in high-latitude regions. At

587 high latitudes (50° - 70°N), GFED4s, QFED2.5, and FINN1.5 identify more forests than VFEI0

588 (Fig. S1) because the former three classify some shrubs (e.g., closed shrublands and woody savanna)

589 as forests, while the latter classify them as grassland. Forests contribute to 70% and more of the

590 comprehensive EFs at high latitudes in the first three emission inventories, but only 8% to the

591 comprehensive EF in VFEI0. The remaining gap in the absolute contribution of forests is caused by

592 the difference in the selected emission factors and the horizontal resolution of the satellite products.

593 **3.5 Contribution of DM and EFs to differences in OC emissions**

594   The above analysis completes the comparison of gaseous pollutant CO among different emission

595 inventories. In this section, we will take OC as an example to compare the emission differences of

596 particulate pollutants. As shown in Fig. 7, the global OC emissions of four datasets range from 14.9

597 to 42.9Tg, with the highest emissions from QFED2.5, which is consistent with previous studies

598 (Carter et al., 2020; Pan et al., 2020). According to the statistical method in section 3.1, we

599 quantified the magnitude of OC emission differences between regions and ranked them as follows:

600 BONA>BOAS>NHAF>SHAF>SEAS>SHSA>EQAS. Compared to the CO emission differences

601 (Fig. 2), the difference in OC emissions becomes larger for BOAS and smaller for low latitude

602 regions of SEAS and EQAS. Since DM should be consistent in the same emission inventories for a

603 given time and area, the magnitude of emissions for different species depends on changes in

604 emission factors. Considering that the emission factors of aerosol-related emission species such as

605 OC, BC, NH_3, SO_2 and $PM_{2.5}$ have been corrected based on the satellite retrieved AOD of the

606 QFED2.5 emission inventory (Table 2), the EFs of OC in QFED2.5 are much higher than that of the

607 other three emission inventories (Fig. 7b). As a result, the OC EFs in the QFED2.5 emission

608 inventory were enlarged by a factor of 1.8-4.5 times through the correction of BOAS, SEAS and

609 EQAS (Table 2). In contrast, the other three emission inventories were not corrected for OC EFs.

610   Unlike the CO EFs, the OC EFs of GFED4s in equatorial regions are largely consistent with the

611   FINN1.5 and VFEI0 emission inventories. Although burning organic matter-rich soil substrates is
612   generally thought to release large amounts of CO, their ability to release OC is similar to that of
613   vegetation such as shurb and some forests. Thus, despite CO emissions bias in EQAS being largely
614   affected by peatlands, differences in OC emissions among the four inventories are not significant.

615   Compared with Pan et al. (2020), it is obvious that the top-down approach will not lead to an
616   increase in emission deviation of the particulate-phase species. The correction of EFs, however, is
617   the root cause of the increased bias in OC emissions. Pan et al. (2020) reported that QFED2.5 and
618   FEER1.0 had the highest global OC emissions, while GFAS1.2 had much lower OC emissions. In
619   this study, the largest OC emission also appears in QFED2.5, but the global total OC emissions of
620   the recently released VFEI0 are relatively low.

621   4 Model evaluation based on emission inventories application

622   4.1 Comparison of simulations with MOPITT CO

623   One of the main goals of this study is to provide a confidence assessment of the BB emission
624   inventories by comparing model simulations with observations. A comparison between model
625   simulations using different emission inventories and ground-based/satellite retrieved data for the
626   respective fire seasons (Table 3) of the main BB regions is explored below. In this study, we
627   compared the model results with measurements from two perspectives: the spatial distribution of
628   BB pollutants, and the time-varying characteristics of BB pollutants.

629   Figure 8 depicts the spatial distribution of CO column burdens in SHSA and SHAF during the
630   fire seasons. In SHSA, the simulated CO column burdens using different emission inventories are
631   all consistent with the spatial distribution pattern of MOPITT CO column burden, with the peak
632   value located in the Amazon rainforest. However, the central value of MOPITT CO column burden
633   is as high as 2.8×10^{18} molecules cm^{-2}, which is slightly higher than the simulated results. Among
634   the four sets of emission inventories, the peak amplitude and spatial distribution of simulated CO
635   column burdens are closest to the satellite retrieved data after applying the GFED4s and VFEI0. In
636   SHAF, however, the model underestimated the peak CO column burden after applying all emission
637   inventories except VFEI0.

638   In addition to SHSA and SHAF, a comparison of regionally averaged CO column burdens
639   between our simulations and MOPITT CO in major BB regions is also shown in Table 3. In the
640   Northern Hemisphere, our simulations are significantly underestimated compared to MOPITT CO,
641   while those in the Southern Hemisphere are consistent with satellite retrievals. Surprisingly, the
642   simulated spatial distributions and magnitudes of CO in the Southern Hemisphere using the recently
643   released VFEI0 agree very well with observations. In contrast, the underestimation of CO
644   concentrations in the Northern Hemisphere is partly due to uncertainty in anthropogenic emissions,
645   as we assume anthropogenic emissions at 2010 levels, which are lower than those during the 2013-
646   2016 period.

647   Note that simulated CO concentrations are 30-40% lower than MOPITT CO at high latitudes.
648   Besides the impact of emission inventories, there are also large uncertainties in satellite-retrieved
649   CO concentrations (Lin et al., 2020a; Pan et al., 2020). In addition, OH loss, long-range transport,
650   and photochemical reactions involved in the CESM2-CAM6 model simulations also lead to
651   uncertainties in simulated CO. For example, MOZART-4x contains an additional OH oxidation
652   pathway for CO, which may lead to lower CO concentrations (Lamarque et al., 2012; He and Zhang,

653   2014; Barré et al., 2015; Brown-Steiner et al., 2018; Emmons et al., 2020). In comparison, the
654   simulated CO by using GFED4s is closest to the MOPITT CO value in terms of spatial distribution
655   and peak magnitude at high latitudes in Northern Hemisphere, which is superior to other emission
656   inventories.

4.2 Comparison of simulations with MODIS AOD

658   We compared MODIS-derived aerosol optical depth (AOD) data with simulated AOD in major
659   BB areas. Figure 9 shows the spatial distribution of AOD in SHSA and SHAF during their fire
660   seasons. The simulated AOD is significantly higher than the MODIS AOD in SHSA. Note that
661   primary organic aerosols (POA) associated with BB account for only 15-23% of the total AOD in
662   Amazon, while secondary organic aerosols (SOA) account for approximately 50% of the total AOD.
663   Furthermore, overestimation of simulated AOD occurs throughout the year, not just during the fire
664   season. Considering the high biogenic emissions in this region, the overestimation of AOD could
665   be attributed to the formation of biogenic SOA. In SHAF, the spatial distribution and magnitude of
666   simulated AOD using GFED4s and VFEI0 are close to those of the MODIS AOD. In comparison,
667   our results show that AOD is significantly underestimated using FINN1.5, but largely overestimated
668   using QFED2.5.

669   Table 4 shows the mean values of model-simulated AOD and satellite measurements for each
670   region during its fire season. The influence of the BB emission inventory has little effect on the
671   simulated AOD value in the Southern Hemisphere, and the regional average AOD deviation is
672   within 20%. In contrast, the average deviation of simulated AOD driven by four BB inventories can
673   be as high as 40% in the high latitudes of the Northern Hemisphere. Comparatively, GFED4s and
674   QFED2.5 are more suited for high latitudes in the northern hemisphere, whereas the VFEI0 is most
675   suitable for the southern hemisphere for AOD simulations. In Africa, QFED2.5 is not recommended
676   due to its considerable overestimation.

4.3 Comparison of simulations with ground-based measurements

678   In the above sections we merely discussed the spatial distribution and the magnitude of pollutants
679   during fire seasons. To further analyze whether each dataset can effectively capture the
680   instantaneous combustion of BB, we compared the value of simulated daily AOD with that of
681   ground-based observation (Fig. 10). In order to be more representative, we selected stations in each
682   BB region with a large amount of data during fire season, allowing a comprehensive assessment of
683   the global BB emission inventories. The specific locations of the selected 12 AERONET sites are
684   shown as red triangles in Fig. 1b.

685   At EQAS sites such as Palangkaraya and Jambi, the observed AOD from September to November
686   in 2014/2015 is generally higher than 1, with peaks exceeding 5, reflecting the intense BB events
687   (Fig. 10a-b). Only simulations using GFED4s are consistent with observed AOD during strong BB
688   events, with a slight underestimation of 33-38%, while none of the other simulations could capture
689   the BB process. Considering the significant contribution of peatlands to BB emissions in EQAS in
690   GFED4s, our results suggest that it is important to include the burning of organic matter-rich soils
691   in BB emission inventories. At SEAS sites such as Omkoi and Ubon Ratchathani, the peak AOD
692   occurs from February to April at a value of about 2, and all simulations applying the four emission
693   inventories capture the observed changes in AOD (Fig 10c-d). However, due to the uncertainty of

694   anthropogenic emissions, the simulated AOD is usually smaller than the actual observed value in
695   EQAS. Note that simulations using QFED2.5 are most consistent with observed AOD during intense
696   biomass burning events.
697   At the Namibe station of SHAF (Fig. 10e), the simulated AOD agrees best with the measured
698   results after using FINN1.5 and GFED2.5, with NMB values within ±8%, indicating these two
699   emission inventories can characterize the day-to-day variability of the intense BB process. However,
700   Namibe is located downwind of the dust source, and dust aerosols contribute more than 50% to the
701   total AOD in this area. To better evaluate the performance of the four BB emission inventories in
702   SHAF, we chose another site, Mongu Inn, located in the interior of Southern Hemispheric Africa,
703   where dust and sea salt accounted for 20-30% of the total AOD. At Mongu Inn, all simulations
704   underestimate AOD by 46-71%, and only QFED2.5 and VFEI0 emission inventories are able to
705   capture a few peaks during intense biomass burning events (Fig. 10f). In SHSA, while Figures 9
706   and 10h show an overall overestimation of simulated AOD compared to MODIS AOD, at the
707   Brazilian Alta Floresta site east of the Amazon, simulated AOD agrees very well with the ground-
708   based observations (Fig. 10g). In general, the simulations using the VFEI0 emission inventory for
709   the Southern Hemisphere are close to the measurements.
710   At high latitudes, simulations driven by GFED4s and QFED2.5 better capture the observed peak
711   AOD, with regional NMB values of less than 40% (Fig. 10i-l), suggesting that these two simulations
712   can reproduce the intense BB process. In contrast, FINN1.5 and VFEI0 are obviously not suitable
713   for describing the BB process in these sites, and the simulated AOD is underestimated by 60-80%.

714   **5 Conclusion and Discussion**

715   The establishment of BB emission inventories follows two basic approaches, one is a "bottom-
716   up" approach, which usually establishes inventory information based on observed surface data (such
717   as detected fire points, burned area, and vegetation types). The other one is a "top-down" approach,
718   that is, the vegetation consumption is inversely calculated from the radiative energy release rate of
719   vegetation burning observed by satellite, and the vegetation type information is superimposed to
720   establish the inventory. In this study, four commonly used BB emission inventories are chosen to
721   understand the uncertainty of BB emissions, two of which are bottom-up inventories (GFED4s and
722   FINN1.5), and two are top-down inventories (QFED2.5 and VFEI0). We analyze the differences in
723   CO and OC emissions from these inventories for seven major BB regions around the world from
724   2013 to 2016. We explore the differences between gaseous and particulate emission inventories and
725   quantify the impact of vegetation classification, cloud cover, and emission factors on emission
726   inventory bias. We also applied the four BB emission inventories to the global model CESM2-
727   CAM6 to assess the model's ability to simulate pollutants, by comparing the simulations with
728   measurements from satellite products or ground-based observations.
729   The total global CO emissions in the four inventories vary greatly, with their annual average
730   values fluctuating between 252-336 Tg, and the maximum deviation rate exceeds 30%. In some
731   regions, changes in CO emissions are even larger. For example, GFED4s in BONA emits 5.8 times
732   more CO emissions than FINN1.5, while the coefficient variation of the four emission inventories
733   in EQAS is as high as 0.67. Overall, CO emissions from GFED4s are higher than those from VFEI0
734   and QFED2.5 inventories in all regions, with the lowest CO emissions in FINN1.5 inventory. DM
735   dominates the variance among BB emission inventories, accounting for 50-80% of the regional bias,
736   while comprehensive EFs account for the remaining 20-50%. Notably, the contribution of DM and

737 comprehensive EFs to the differences in BB emission inventories are comparable across equatorial
738 regions and Northern Hemisphere high latitudes.
739   There is a large uncertainty in DM due to the calculation of underlying fuel consumption and
740 burned area, which in turn is related to the vegetation classification method, fire detection product
741 algorithm, and cloud/smoke masking used in the emission inventory. First, the vegetation
742 classification method affects fuel loading and the Fraction of Biomass burned. At low latitudes
743 (except Southeast Asia), the fuel consumption term of FINN1.5 is less than 50% of that of GFED4s,
744 where the vegetation classification method contributes significantly to this bias. For example, in
745 EQAS, while GFED4s classifies a significant protion of the area as peatland, FINN1.5 identifies it
746 as grassland, resulting in 37% lower fuel consumption for FINN1.5 than GFED4s in this region. In
747 addition, GFED4s assumes that the FB of tropical forest is 40-60%, while FINN1.5 assumes that
748 the FB of forests does not exceed 30%, so the FB of forests in FINN1.5 is 25-50% lower than
749 GFED4s. Similarly, the fuel consumption of FINN1.5 in high latitudes is also lower than that of
750 GFED4s, with a deviation of up to 50% or more. The classification of peatlands, the amount of
751 forest burnable (fuel load) and burning percentage of the forest remain the main contributions.
752 Second, different fire detection products can also cause bias in the estimated burned area, leading
753 to uncertainty in DM. For example, the MCD14DL used in FINN1.5 identifies fire points based on
754 brightness temperature, which can effectively detect understory burns in tropical rainforests, and
755 can easily capture small area burns in agricultural fields. Furthermore, combined with the smoothing
756 assumptions for equatorial regions, the estimated burned area in FINN1.5 is generally larger than
757 that in GFED4s at low latitudes. Last but not least, satellite transit/cloud obscuration can similarly
758 affect DM between emission inventories by influencing the identification of burned area/fire
759 radiative energy. In the Africa grasslands where fires develop rapidly, due to the fast fuel
760 consumption, the burned area often has a large difference in a short period of time. If the fire point
761 monitoring product based on brightness temperature data identification is used, there may be missed
762 detections of fire that occur during the satellite transit/cloud occlusion, but fire area product
763 indentified based on surface albedo changes can better avoid missed detections caused by satellite
764 transit/cloud occlusion. Cloud cover at high latitudes has a significant impact on the uncertainty of
765 emission inventories. According to our results, the bias between bottom-up (or top-down) emission
766 inventories in BONA increased by 20% in July with increased cloud fraction.
767   In addition to gaseous emissions, we also analyzed the differences in emissions of particulate
768 pollutants among emission inventories using OC as an example. The four sets of BB emission
769 inventories fluctuate between 14.9 and 42.9 Tg of global average annual OC emissions, a greater
770 variation than the gaseous species CO. Similar to the results for CO emission variability, current BB
771 emission inventories have large variability at high northern latitudes. Unlike differences in CO
772 emissions, there is less variability in comprehensive EFs over the equator. In particular, the
773 QFED2.5 inventory adjusted emission factors using satellite aerosol optical thickness (AOD) to
774 enhance emissions of particulate matter including OC. In addition, peatlands only have comparable
775 OC emission capacity to the shrub, which makes the impact of vegetation classification differences
776 on OC EFs less significant, ultimately resulting in lower variability in particle-phase emissions in
777 equatorial regions.
778   We applied four sets of BB emission inventories to CESM2-CAM6 and compared the model-
779 simulated CO column concentrations with the MOPITT satellite inversion CO column
780 concentrations. According to our simulations, CO simulated using GFED4s is closest to satellite

19

781   observations in almost all regions except southern Asia and Africa. We also compared model results
782   with AOD retrieved from MODIS satellites or measured by AERONET. Simulated AOD at high
783   northern latitudes is often underestimated when using current mainstream BB emission inventories.
784   For example, the simulated regional average AOD is 8-46% lower than MODIS in North America.
785   Unlike the high latitudes, the simulated AOD is significantly overestimated at the equator, and the
786   regional average AOD simulated by the model in Northern Hemispheric Africa is 66-91% higher
787   than MODIS. In addition, comparing model simulated AOD with AERONET ground-based
788   observations, we find that GFED4s performs best in EQAS for daily variability during intense
789   burning. In SEAS, although FINN1.5 can better represent the magnitude of the overall OC
790   emissions in the BB season, QFED2.5 can capture the day-to-day variation characteristics of intense
791   combustion. In the Southern Hemisphere, the latest VFEI0 emission inventory performs well, and
792   the simulated AOD is able to capture the BB processes.

793   Our study assesses the global applicability of BB emission inventories and has some implications
794   for future study. Overall, GFED4s and QFED2.5 inventories for the northern high latitudes capture
795   the magnitude and daily variation of OC emitted throughout the BB season. These two emission
796   inventories outperformed the others when applied to studies of interactions between BB aerosol and
797   weather/climate. In the Southern Hemisphere, the spatial distribution and daily variation
798   characteristics of CO and AOD simulated by the model are closest to the observed values when the
799   latest VFEI0 emission inventory is applied. For the equator, the situation is more complicated, and
800   we recommend combining emission inventories according to the research objectives. For example,
801   GFED4s performs best in day-to-day changes during intense burning in equatorial Asia. In
802   Southeast Asia, combining OC magnitude in FINN1.5 and daily variation in QFED2.5 is the optimal
803   choice.

804

805   *Data availability.* The biomass burning emission datasets used in this work are available from
806   http://www.globalfifiredata.org   (GFED4s),   https://www.acom.ucar.edu/Data/fire/   (FINN1.5),
807   https://portal.nccs.nasa.gov/datashare/iesa/aerosol/emissions/QFED/v2.5r1/   (QFED2.5),   and
808   http://bio.cgrer.uiowa.edu/VFEI/DOWNLOAD/ (VFEI0). AOD and cloud fraction from MODIS
809   dataset can be obtained from https://ladsweb.modaps.eosdis.nasa.gov/search/. MOPITT CO can be
810   obtained   from   https://doi.org/10.5067/TERRA/MOPITT/MOP03JM.009.   AERONET   AOD   is
811   avaiable from https://aeronet.gsfc.nasa.gov/new_web/download_all_v3_aod.html. The Modern-Era
812   Retrospective analysis for Research and Applications, version 2 (MERRA-2) reanalysis data is
813   available   from   https://gmao.gsfc.nasa.gov/reanalysis/MERRA-2/.   All data analyzed during the
814   current study are included in this published article and its supplementary information. Raw model
815   simulations are available from the corresponding author on reasonable request.

816

817

818   *Author contributions.* S. L. and A. D. designed the research, W. H. and S. L. conducted the data
819   analysis and model simulations, W. H. and S. L. took the lead in writing the manuscript, with
820   contributions from all authors.

821

822   *Competing interests.* The authors declare that they have no conflict of interest.

823

831
832

833   **References**

834   Adams, C., McLinden, C. A., Shephard, M. W., Dickson, N., Dammers, E., Chen, J., Makar, P., Cady-
835   Pereira, K. E., Tam, N., and Kharol, S. K.: Satellite-derived emissions of carbon monoxide, ammonia,
836   and nitrogen dioxide from the 2016 Horse River wildfire in the Fort McMurray area, Atmospheric
837   Chemistry and Physics, 19, 2577-2599, 2019.
838   Akagi, S., Yokelson, R. J., Wiedinmyer, C., Alvarado, M., Reid, J., Karl, T., Crounse, J., and Wennberg,
839   P.: Emission factors for open and domestic biomass burning for use in atmospheric models, Atmospheric
840   Chemistry and Physics, 11, 4039-4072, 2011.
841   Alencar, A., Nepstad, D., and Moutinho, P.: Carbon emissions associated with forest fires in Brazil,
842   Tropical deforestation and climate change, 23, 2005.
843   Alvarado, M., Logan, J., Mao, J., Apel, E., Riemer, D., Blake, D., Cohen, R., Min, K.-E., Perring, A.,
844   and Browne, E.: Nitrogen oxides and PAN in plumes from boreal fires during ARCTAS-B and their
845   impact on ozone: an integrated analysis of aircraft and satellite observations, Atmospheric Chemistry
846   and Physics, 10, 9739-9760, 2010.
847   Andreae, M. and Rosenfeld, D.: Aerosol–cloud–precipitation interactions. Part 1. The nature and sources
848   of cloud-active aerosols, Earth-Science Reviews, 89, 13-41, 2008.
849   Andreae, M. O.: Emission of trace gases and aerosols from biomass burning–an updated assessment,
850   Atmospheric Chemistry and Physics, 19, 8523-8546, 2019.
851   Andreae, M. O. and Merlet, P.: Emission of trace gases and aerosols from biomass burning, Global
852   biogeochemical cycles, 15, 955-966, 2001.
853   Arellano Jr, A. F. and Hess, P. G.: Sensitivity of top‐down estimates of CO sources to GCTM transport,
854   Geophysical Research Letters, 33, 2006.
855   Arellano Jr, A. F., Kasibhatla, P. S., Giglio, L., van der Werf, G. R., and Randerson, J. T.: Top‐down
856   estimates of global CO sources using MOPITT measurements, Geophysical research letters, 31, 2004.
857   Balshi, M. S., McGuire, A. D., Duffy, P., Flannigan, M., Kicklighter, D. W., and Melillo, J.: Vulnerability
858   of carbon storage in North American boreal forests to wildfires during the 21st century, Global change
859   biology, 15, 1491-1510, 2009.
860   Barré, J., Gaubert, B., Arellano, A. F., Worden, H. M., Edwards, D. P., Deeter, M. N., Anderson, J. L.,
861   Raeder, K., Collins, N., and Tilmes, S.: Assessing the impacts of assimilating IASI and MOPITT CO
862   retrievals using CESM‐CAM‐chem and DART, Journal of Geophysical Research: Atmospheres, 120,
863   10,501-510,529, 2015.
864   Beck, H. E., Zimmermann, N. E., McVicar, T. R., Vergopolan, N., Berg, A., and Wood, E. F.: Present and
865   future Köppen-Geiger climate classification maps at 1-km resolution, Scientific data, 5, 1-12, 2018.

866   Bian, H., Chin, M., Kawa, S., Duncan, B., Arellano, A., and Kasibhatla, P.: Sensitivity of global CO
867   simulations to uncertainties in biomass burning sources, Journal of Geophysical Research: Atmospheres,
868   112, 2007.
869   Boschetti, L., Roy, D. P., Justice, C. O., and Humber, M. L.: MODIS–Landsat fusion for large area 30 m
870   burned area mapping, Remote Sensing of Environment, 161, 27-42, 2015.
871   Boschetti, L., Roy, D. P., Giglio, L., Huang, H., Zubkova, M., and Humber, M. L.: Global validation of
872   the collection 6 MODIS burned area product, Remote sensing of environment, 235, 111490, 2019.
873   Boucher, O., Randall, D., Artaxo, P., et al.: Clouds and aerosols, Climate change 2013: The physical
874   science basis, Contribution of working group I to the fifth assessment report of the intergovernmental
875   panel on climate change, Cambridge University Press, 571-657, 2013.
876   Brando, P. M., Soares-Filho, B., Rodrigues, L., Assunção, A., Morton, D., Tuchschneider, D., Fernandes,
877   E., Macedo, M., Oliveira, U., and Coe, M.: The gathering firestorm in southern Amazonia, Science
878   Advances, 6, eaay1632, 2020.
879   Brown-Steiner, B., Selin, N. E., Prinn, R., Tilmes, S., Emmons, L., Lamarque, J.-F., and Cameron-Smith,
880   P.: Evaluating simplified chemical mechanisms within present-day simulations of the Community Earth
881   System Model version 1.2 with CAM4 (CESM1. 2 CAM-chem): MOZART-4 vs. Reduced Hydrocarbon
882   vs. Super-Fast chemistry, Geoscientific Model Development, 11, 4155-4174, 2018.
883   Carter, T. S., Heald, C. L., Jimenez, J. L., Campuzano-Jost, P., Kondo, Y., Moteki, N., Schwarz, J. P.,
884   Wiedinmyer, C., Darmenov, A. S., and da Silva, A. M.: How emissions uncertainty influences the
885   distribution and radiative impacts of smoke from fires in North America, Atmospheric Chemistry and
886   Physics, 20, 2073-2097, 2020.
887   Chen, Y., Li, Q., Randerson, J., Lyons, E., Kahn, R., Nelson, D., and Diner, D.: The sensitivity of CO
888   and aerosol transport to the temporal and vertical distribution of North American boreal fire emissions,
889   Atmospheric Chemistry and Physics, 9, 6559-6580, 2009.
890   Christian, T. J., Kleiss, B., Yokelson, R. J., Holzinger, R., Crutzen, P. J., Hao, W. M., Saharjo, B. H., and
891   Ward, D. E.: Comprehensive laboratory measurements of biomass‐burning emissions: 1. Emissions
892   from Indonesian, African, and other fuels, Journal of Geophysical Research: Atmospheres, 108(D23),
893   2003.
894   Christian, K., Wang, J., Ge, C., Peterson, D., Hyer, E., Yorks, J., and McGill, M.: Radiative forcing and
895   stratospheric warming of pyrocumulonimbus smoke aerosols: First modeling results with multisensor
896   (EPIC, CALIPSO, and CATS) views from space, Geophysical Research Letters, 46, 10061-10071, 2019.
897   Cochrane, M. A.: Fire science for rainforests, Nature, 421, 913-919, 2003.
898   Cochrane, M. A. and Laurance, W. F.: Fire as a large-scale edge effect in Amazonian forests, Journal of
899   Tropical Ecology, 18, 311-325, 2002.
900   Danabasoglu, G., Lamarque, J. F., Bacmeister, J., Bailey, D., DuVivier, A., Edwards, J., Emmons, L.,
901   Fasullo, J., Garcia, R., and Gettelman, A.: The community earth system model version 2 (CESM2),
902   Journal of Advances in Modeling Earth Systems, 12, e2019MS001916, 2020.
903   Darmenov, A., da Silvia, A., and Koster, R.: The Quick Fire Emissions Dataset (QFED): Documentation
904   of Versions 2.1, 2.2 and 2.4. Volume 38; Technical Report Series on Global Modeling and Data
905   Assimilation, 2015.
906   Deeter, M., Francis, G., Gille, J., Mao, D., Martínez-Alonso, S., Worden, H., Ziskin, D., Drummond, J.,
907   Commane, R., and Diskin, G.: The MOPITT Version 9 CO product: sampling enhancements and
908   validation, Atmospheric Measurement Techniques, 15, 2325-2344, 2022.

909 Ding, K., Huang, X., Ding, A., Wang, M., Su, H., Kerminen, V.-M., Petäjä, T., Tan, Z., Wang, Z., and
910 Zhou, D.: Aerosol-boundary-layer-monsoon interactions amplify semi-direct effect of biomass smoke on
911 low cloud formation in Southeast Asia, Nature communications, 12, 1-9, 2021.
912 Duncan, B. N., Martin, R. V., Staudt, A. C., Yevich, R., and Logan, J. A.: Interannual and seasonal
913 variability of biomass burning emissions constrained by satellite observations, Journal of Geophysical
914 Research: Atmospheres, 108, ACH 1-1-ACH 1-22, 2003.
915 Emmons, L.: Coauthors, 2020: The chemistry mechanism in the community earth system model version
916 2 (CESM2), J. Adv. Model. Earth Syst, 12, e2019MS001882, 2020.
917 Ferek, R. J., Reid, J. S., Hobbs, P. V., Blake, D. R., and Liousse, C.: Emission factors of hydrocarbons,
918 halocarbons, trace gases and particles from biomass burning in Brazil, Journal of Geophysical Research:
919 Atmospheres, 103, 32107-32118, 1998.
920 Ferrada, G. A., Zhou, M., Wang, J., Lyapustin, A., Wang, Y., Freitas, S. R., and Carmichael, G. R.:
921 Introducing the VIIRS-based Fire Emission Inventory version 0 (VFEIv0), Geoscientific Model
922 Development, 15, 8085-8109, 2022.
923 Firms, L.: Collection 6 NRT hotspot/active fire detections MCD14DL, En ligne: https://earthdata. nasa.
924 gov/firms (visité le 21 June 2017), 2017.
925 Freitas, S., Longo, K., and Andreae, M.: Impact of including the plume rise of vegetation fires in
926 numerical simulations of associated atmospheric pollutants, Geophysical Research Letters, 33, 2006.
927 Freitas, S., Longo, K., Trentmann, J., and Latham, D.: Sensitivity of 1-D smoke plume rise models to the
928 inclusion of environmental wind drag, Atmospheric Chemistry and Physics, 10, 585-594, 2010.
929 Friedl, M. A., Sulla-Menashe, D., Tan, B., Schneider, A., Ramankutty, N., Sibley, A., and Huang, X.:
930 MODIS Collection 5 global land cover: Algorithm refinements and characterization of new datasets,
931 Remote sensing of Environment, 114, 168-182, 2010.
932 GMAO: MERRA‐2 inst3_3d_asm_Np: 3d, 3‐hourly, instantaneous, pressure‐level, assimilation,
933 assimilated meteorological fields V5. 12.4, 2015.
934 Gibson, C. M., Chasmer, L. E., Thompson, D. K., Quinton, W. L., Flannigan, M. D., and Olefeldt, D.:
935 Wildfire as a major driver of recent permafrost thaw in boreal peatlands, Nature communications, 9,
936 3041, 2018.
937 Giglio, L., Randerson, J. T., and van der Werf, G. R.: Analysis of daily, monthly, and annual burned area
938 using the fourth‐generation global fire emissions database (GFED4), Journal of Geophysical Research:
939 Biogeosciences, 118, 317-328, 2013.
940 Guenther, A., Jiang, X., Heald, C. L., Sakulyanontvittaya, T., Duhl, T. a., Emmons, L., and Wang, X.:
941 The Model of Emissions of Gases and Aerosols from Nature version 2.1 (MEGAN2. 1): an extended and
942 updated framework for modeling biogenic emissions, Geoscientific Model Development, 5, 1471-1492,
943 2012.
944 He, J. and Zhang, Y.: Improvement and further development in CESM/CAM5: gas-phase chemistry and
945 inorganic aerosol treatments, Atmospheric Chemistry and Physics, 14, 9171-9200, 2014.
946 Hoelzemann, J. J., Schultz, M. G., Brasseur, G. P., Granier, C., and Simon, M.: Global Wildland Fire
947 Emission Model (GWEM): Evaluating the use of global area burnt satellite data, Journal of Geophysical
948 Research: Atmospheres, 109, 2004.
949 Hoesly, R. M., Smith, S. J., Feng, L., Klimont, Z., Janssens-Maenhout, G., Pitkanen, T., Seibert, J. J., Vu,
950 L., Andres, R. J., and Bolt, R. M.: Historical (1750–2014) anthropogenic emissions of reactive gases and
951 aerosols from the Community Emissions Data System (CEDS), Geoscientific Model Development, 11,
952 369-408, 2018.

953   Holben, B. N., Eck, T. F., Slutsker, I. a., Tanre, D., Buis, J., Setzer, A., Vermote, E., Reagan, J. A.,
954   Kaufman, Y., and Nakajima, T.: AERONET—A federated instrument network and data archive for
955   aerosol characterization, Remote sensing of environment, 66, 1-16, 1998.

956   Huang, X., Ding, K., Liu, J., Wang, Z., Tang, R., Xue, L., Wang, H., Zhang, Q., Tan, Z.-M., Fu, C., Davis,
957   S. J., Andreae, M. O., and Ding, A.: Smoke-weather interaction affects extreme wildfires in diverse
958   coastal regions, Science, 379, 457-461, doi:10.1126/science.add9843, 2023.

959   Ichoku, C. and Ellison, L.: Global top-down smoke-aerosol emissions estimation using satellite fire
960   radiative power measurements, Atmospheric Chemistry and Physics, 14, 6643-6667, 2014.

961   Jiang, Y., Yang, X.-Q., Liu, X., Qian, Y., Zhang, K., Wang, M., Li, F., Wang, Y., and Lu, Z.: Impacts of
962   wildfire aerosols on global energy budget and climate: The role of climate feedbacks, Journal of Climate,
963   33, 3351-3366, 2020.

964   Junghenn Noyes, K. T., Kahn, R. A., Limbacher, J. A., and Li, Z.: Canadian and Alaskan wildfire smoke
965   particle properties, their evolution, and controlling factors, from satellite observations, Atmospheric
966   Chemistry and Physics, 22, 10267-10290, 2022.

967   Kaiser, J., Heil, A., Andreae, M., Benedetti, A., Chubarova, N., Jones, L., Morcrette, J.-J., Razinger, M.,
968   Schultz, M., and Suttie, M.: Biomass burning emissions estimated with a global fire assimilation system
969   based on observed fire radiative power, Biogeosciences, 9, 527-554, 2012.

970   Kasischke, E. S. and Bruhwiler, L. P.: Emissions of carbon dioxide, carbon monoxide, and methane from
971   boreal forest fires in 1998, Journal of Geophysical Research: Atmospheres, 107, FFR 2-1-FFR 2-14,
972   2002.

973   Kiely, L., Spracklen, D., Arnold, S., Papargyropoulou, E., Conibear, L., Wiedinmyer, C., Knote, C., and
974   Adrianto, H.: Assessing costs of Indonesian fires and the benefits of restoring peatland, Nature
975   communications, 12, 7044, 2021.

976   Knorr, W., Dentener, F., Hantson, S., Jiang, L., Klimont, Z., and Arneth, A.: Air quality impacts of
977   European wildfire emissions in a changing climate, Atmospheric Chemistry and Physics, 16, 5685-5703,
978   2016.

979   Lamarque, J.-F., Emmons, L., Hess, P., Kinnison, D. E., Tilmes, S., Vitt, F., Heald, C., Holland, E. A.,
980   Lauritzen, P., and Neu, J.: CAM-chem: Description and evaluation of interactive atmospheric chemistry
981   in the Community Earth System Model, Geoscientific Model Development, 5, 369-411, 2012.

982   Lin, C., Cohen, J. B., Wang, S., and Lan, R.: Application of a combined standard deviation and mean
983   based approach to MOPITT CO column data, and resulting improved representation of biomass burning
984   and urban air pollution sources, Remote Sensing of Environment, 241, 111720, 2020a.

985   Lin, C., Cohen, J. B., Wang, S., Lan, R., and Deng, W.: A new perspective on the spatial, temporal, and
986   vertical distribution of biomass burning: quantifying a significant increase in CO emissions,
987   Environmental Research Letters, 15, 104091, 2020b.

988   Liousse, C., Guillaume, B., Grégoire, J.-M., Mallet, M., Galy, C., Pont, V., Akpo, A., Bedou, M., Castéra,
989   P., and Dungall, L.: Updated African biomass burning emission inventories in the framework of the
990   AMMA-IDAF program, with an evaluation of combustion aerosols, Atmospheric Chemistry and Physics,
991   10, 9631-9646, 2010.

992   Liu, L., Cheng, Y., Wang, S., Wei, C., Pöhlker, M. L., Pöhlker, C., Artaxo, P., Shrivastava, M., Andreae,
993   M. O., and Pöschl, U.: Impact of biomass burning aerosols on radiation, clouds, and precipitation over
994   the Amazon: relative importance of aerosol–cloud and aerosol–radiation interactions, Atmospheric
995   Chemistry and Physics, 20, 13283-13301, 2020a.

996   Liu, T., Mickley, L. J., Marlier, M. E., DeFries, R. S., Khan, M. F., Latif, M. T., and Karambelas, A.:
997   Diagnosing spatial biases and uncertainties in global fire emissions inventories: Indonesia as regional
998   case study, Remote Sensing of Environment, 237, 111557, 2020b.
999   Liu, X., Ma, P.-L., Wang, H., Tilmes, S., Singh, B., Easter, R., Ghan, S., and Rasch, P.: Description and
1000   evaluation of a new four-mode version of the Modal Aerosol Module (MAM4) within version 5.3 of the
1001   Community Atmosphere Model, Geoscientific Model Development, 9, 505-522, 2016.
1002   Liu, Y., Zhang, K., Qian, Y., Wang, Y., Zou, Y., Song, Y., Wan, H., Liu, X., and Yang, X.-Q.: Investigation
1003   of short-term effective radiative forcing of fire aerosols over North America using nudged hindcast
1004   ensembles, Atmospheric Chemistry and Physics, 18, 31-47, 2018.
1005   McMeeking, G. R., Kreidenweis, S. M., Baker, S., Carrico, C. M., Chow, J. C., Collett Jr, J. L., Hao, W.
1006   M., Holden, A. S., Kirchstetter, T. W., and Malm, W. C.: Emissions of trace gases and aerosols during
1007   the open combustion of biomass in the laboratory, Journal of Geophysical Research: Atmospheres, 114,
1008   2009.
1009   Mieville, A., Granier, C., Liousse, C., Guillaume, B., Mouillot, F., Lamarque, J.-F., Grégoire, J.-M., and
1010   Pétron, G.: Emissions of gases and particles from biomass burning during the 20th century using satellite
1011   data and an historical reconstruction, Atmospheric Environment, 44, 1469-1477, 2010.
1012   Neu, J. and Prather, M.: Toward a more physical representation of precipitation scavenging in global
1013   chemistry models: cloud overlap and ice physics and their impact on tropospheric ozone, Atmospheric
1014   Chemistry and Physics, 12, 3289-3310, 2012.
1015   Olson, D. M., Dinerstein, E., Wikramanayake, E. D., Burgess, N. D., Powell, G. V., Underwood, E. C.,
1016   D'amico, J. A., Itoua, I., Strand, H. E., and Morrison, J. C.: Terrestrial Ecoregions of the World: A New
1017   Map of Life on EarthA new global map of terrestrial ecoregions provides an innovative tool for
1018   conserving biodiversity, BioScience, 51, 933-938, 2001.
1019   Page, S. E., Siegert, F., Rieley, J. O., Boehm, H.-D. V., Jaya, A., and Limin, S.: The amount of carbon
1020   released from peat and forest fires in Indonesia during 1997, Nature, 420, 61-65, 2002.
1021   Pan, X., Ichoku, C., Chin, M., Bian, H., Darmenov, A., Colarco, P., Ellison, L., Kucsera, T., da Silva, A.,
1022   and Wang, J.: Six global biomass burning emission datasets: intercomparison and application in one
1023   global aerosol model, Atmospheric Chemistry and Physics, 20, 969-994, 2020.
1024   Paton-Walsh, C., Emmons, L. K., and Wiedinmyer, C.: Australia's Black Saturday fires–Comparison of
1025   techniques for estimating emissions from vegetation fires, Atmospheric Environment, 60, 262-270, 2012.
1026   Paton‑Walsh, C., Deutscher, N. M., Griffith, D., Forgan, B., Wilson, S., Jones, N., and Edwards, D.:
1027   Trace gas emissions from savanna fires in northern Australia, Journal of Geophysical Research:
1028   Atmospheres, 115, 2010.
1029   Platnick, S., King, M., Meyer, K., Wind, G., Amarasinghe, N., Marchant, B., Arnold, G., Zhang, Z.,
1030   Hubanks, P., and Ridgway, B.: MODIS atmosphere L3 monthly product, NASA MODIS Adaptive
1031   processing system, goddard space flight center, USA, 20, 2015.
1032   Ramnarine, E., Kodros, J. K., Hodshire, A. L., Lonsdale, C. R., Alvarado, M. J., and Pierce, J. R.: Effects
1033   of near-source coagulation of biomass burning aerosols on global predictions of aerosol size distributions
1034   and implications for aerosol radiative effects, Atmospheric Chemistry and Physics, 19, 6561-6577, 2019.
1035   Randerson, J. T., van der Werf, G. R., Giglio, L., Collztz, G. J., and Kasibhatla, P. S.: Global Fire
1036   Emission Database, Version 4.1 (GFEDv4). ORNLDAAC, Oak Ridge, Tennessee, USA, 2018.
1037   https://doi.org/10.3334/ORNLDAAC/1293

1038   Reid, W. V. and Mooney, H. A.: The Millennium Ecosystem Assessment: testing the limits of
1039   interdisciplinary and multi-scale science, Current Opinion in Environmental Sustainability, 19, 40-46,
1040   2016.
1041   Reid, W. V., Mooney, H. A., Cropper, A., Capistrano, D., Carpenter, S. R., Chopra, K., Dasgupta, P.,
1042   Dietz, T., Duraiappah, A. K., and Hassan, R.: Ecosystems and human well-being-Synthesis: A report of
1043   the Millennium Ecosystem Assessment, Island Press, 2005.
1044   Roy, D. P., Boschetti, L., Justice, C., and Ju, J.: The collection 5 MODIS burned area product—Global
1045   evaluation by comparison with the MODIS active fire product, Remote sensing of Environment, 112,
1046   3690-3707, 2008.
1047   Schaefer, K., Collatz, G. J., Tans, P., Denning, A. S., Baker, I., Berry, J., Prihodko, L., Suits, N., and
1048   Philpott, A.: Combined simple biosphere/Carnegie‐Ames‐Stanford approach terrestrial carbon cycle
1049   model, Journal of Geophysical Research: Biogeosciences, 113, 2008.
1050   Spracklen, D., Jimenez, J., Carslaw, K., Worsnop, D., Evans, M., Mann, G., Zhang, Q., Canagaratna, M.,
1051   Allan, J., and Coe, H.: Aerosol mass spectrometer constraint on the global secondary organic aerosol
1052   budget, Atmospheric Chemistry and Physics, 11, 12109-12136, 2011.
1053   Stockwell, T., Zhao, J., Greenfield, T., Li, J., Livingston, M., and Meng, Y.: Estimating under‐and
1054   over‐reporting of drinking in national surveys of alcohol consumption: identification of consistent
1055   biases across four English‐speaking countries, Addiction, 111, 1203-1213, 2016.
1056   Tilmes, S., Hodzic, A., Emmons, L., Mills, M., Gettelman, A., Kinnison, D. E., Park, M., Lamarque, J.
1057   F., Vitt, F., and Shrivastava, M.: Climate forcing and trends of organic aerosols in the Community Earth
1058   System Model (CESM2), Journal of Advances in Modeling Earth Systems, 11, 4323-4351, 2019.
1059   Urbanski, S., Hao, W., and Nordgren, B.: The wildland fire emission inventory: western United States
1060   emission estimates and an evaluation of uncertainty, Atmospheric Chemistry and Physics, 11, 12973-
1061   13000, 2011.
1062   van der Werf, G., Randerson, J., Giglio, L., Collatz, J., Kasibhatla, P., Morton, D., and DeFries, R.: The
1063   improved Global Fire Emissions Database (GFED) version 3: contribution of savanna, forest,
1064   deforestation, and peat fires to the global fire emissions budget, EGU General Assembly Conference
1065   Abstracts, 2010a.
1066   van der Werf, G. R., Randerson, J. T., Giglio, L., Collatz, G. J., Kasibhatla, P. S., and Arellano Jr, A. F.:
1067   Interannual variability in global biomass burning emissions from 1997 to 2004, Atmospheric Chemistry
1068   and Physics, 6, 3423-3441, 2006.
1069   van der Werf, G. R., Randerson, J. T., Giglio, L., Collatz, G., Mu, M., Kasibhatla, P. S., Morton, D. C.,
1070   DeFries, R., Jin, Y. v., and van Leeuwen, T. T.: Global fire emissions and the contribution of deforestation,
1071   savanna, forest, agricultural, and peat fires (1997–2009), Atmospheric chemistry and physics, 10, 11707-
1072   11735, 2010b.
1073   van der Werf, G. R., Randerson, J. T., Giglio, L., van Leeuwen, T. T., Chen, Y., Rogers, B. M., Mu, M.,
1074   van Marle, M. J., Morton, D. C., and Collatz, G. J.: Global fire emissions estimates during 1997–2016,
1075   Earth System Science Data, 9, 697-720, 2017.
1076   Vetrita, Y., Cochrane, M. A., Priyatna, M., Sukowati, K. A., and Khomarudin, M. R.: Evaluating accuracy
1077   of four MODIS-derived burned area products for tropical peatland and non-peatland fires, Environmental
1078   Research Letters, 16, 035015, 2021.
1079   Warner, J. X., Gille, J. C., Edwards, D. P., Ziskin, D. C., Smith, M. W., Bailey, P. L., and Rokke, L.:
1080   Cloud detection and clearing for the Earth Observing System Terra satellite Measurements of Pollution
1081   in the Troposphere (MOPITT) experiment, Applied Optics, 40, 1269-1284, 2001.

1082 Webb, M. J., Andrews, T., Bodas-Salcedo, A., Bony, S., Bretherton, C. S., Chadwick, R., Chepfer, H.,
1083 Douville, H., Good, P., and Kay, J. E.: The cloud feedback model intercomparison project (CFMIP)
1084 contribution to CMIP6, Geoscientific Model Development, 10, 359-384, 2017.
1085 Westerling, A. L. and Bryant, B.: Climate change and wildfire in California, Climatic Change, 87, 231-
1086 249, 2008.
1087 Westerling, A. L., Hidalgo, H. G., Cayan, D. R., and Swetnam, T. W.: Warming and earlier spring increase
1088 western US forest wildfire activity, science, 313, 940-943, 2006.
1089 Wiedinmyer, C., Akagi, S., Yokelson, R. J., Emmons, L., Al-Saadi, J., Orlando, J., and Soja, A.: The Fire
1090 INventory from NCAR (FINN): A high resolution global model to estimate the emissions from open
1091 burning, Geoscientific Model Development, 4, 625-641, 2011.
1092 Wiedinmyer, C., Quayle, B., Geron, C., Belote, A., McKenzie, D., Zhang, X., O'Neill, S., and Wynne,
1093 K. K.: Estimating emissions from fires in North America for air quality modeling, Atmospheric
1094 Environment, 40, 3419-3432, 2006.
1095 Williams, J. E., van Weele, M., van Velthoven, P. F., Scheele, M. P., Liousse, C., and van Der Werf, G.
1096 R.: The impact of uncertainties in African biomass burning emission estimates on modeling global air
1097 quality, long range transport and tropospheric chemical lifetimes, Atmosphere, 3, 132-163, 2012.
1098 Yang, Y., Smith, S. J., Wang, H., Mills, C. M., and Rasch, P. J.: Variability, timescales, and nonlinearity
1099 in climate responses to black carbon emissions, Atmospheric Chemistry and Physics, 19, 2405-2420,
1100 2019.
1101 Yokelson, R. J., Susott, R., Ward, D. E., Reardon, J., and Griffith, D. W. T.: Emissions from smoldering
1102 combustion of biomass measured by open-path Fourier transform infrared spectroscopy, Journal of
1103 Geophysical Research: Atmospheres, 102(D15), 18865-18877, 1997.
1104 Yu, P., Toon, O. B., Bardeen, C. G., Zhu, Y., Rosenlof, K. H., Portmann, R. W., Thornberry, T. D., Gao,
1105 R.-S., Davis, S. M., and Wolf, E. T.: Black carbon lofts wildfire smoke high into the stratosphere to form
1106 a persistent plume, Science, 365, 587-590, 2019.
1107 Zhang, Y., Li, Z., Chen, Y., de Leeuw, G., Zhang, C., Xie, Y., and Li, K.: Improved inversion of aerosol
1108 components in the atmospheric column from remote sensing data, Atmospheric Chemistry and Physics,
1109 20, 12795-12811, 2020.
1110

1111   **Table 1. Brief introduction of four BB inventories**

Inventory	"Bottom-up"		"Top-down"	
	FINN1.5	GFED4s	QFED2.5	VFEI0
Temporal range	2002- (NRT) [a]	1997-2022 [b]	2000- (NRT) [a]	2012- (NRT) [a]
Spatio-temporal resolution	1km, daily	0.25°, monthly (daily fraction)	0.1°, daily (0.25° × 0.375°, NRT [a])	500m, daily
Primary satellite fire input	MCD14DL C5 active fire area (1km)	MCD64A1 C5.1 burned area (500m)	MOD14/MYD14 C6 FRP (1km)	VNP14IMG FRP (1km)
Statistical boosts/Adjustion	Smooth assumption in tropics [c]	Small fire boost (MOD14A1/MYD14A1)	Cloud-gap adjusted FRP density	
Primary land use/land cover (LULC)	MCD12Q1 (IGBP), 2005	MCD12Q1 (UMD), 2001-2012	IGBP-INPE	MCD12C1(IGBP) + The Köppen Climate Classification
Peatland fire	×	Olson et al. (2001)	×	Ferrada et al. (2022)
Conversion to dry matter	Hoelzemann et al. (2004)	CASA biogeochemical model (van der Werf et al., 2010)	QFED FRP vs GFED2 dry matter global calibration	VFEI FRP vs GFED3.1 dry matter global calibration
Emission factors	Akagi et al. (2011), Andreae and Merlet (2001)	Akagi et al. (2011) + updates from Andreae et al. (2013)	Andreae and Merlet (2001), Akagi et al. (2011) [d]	Akagi et al. (2019)
Speciation	41 species	27 species	17 species	46 species
References	Wiedinmyer et al. (2011)	van der Werf et al. (2017)	Darmenov and da Silva (2015)	Ferrada et al. (2022)

1112   a: NRT = near real time;   b: 2017-2022 are beta version releases;

1113   c: In equatorial region (30°N-30°S), each detected fire will be counted as 2-day, assuming the second day's fire will continue to be half the

1114   size of the previous day;

1115   d: Particulate matter-related emissions from biomass burning (e.g. BC, OC, NH_3, SO_2, and $PM_{2.5}$) were corrected from emission factors

1116   based on MODIS AOD.

1117

1118

1119

1120 **Table 2. CO and OC emission factors used in the four biomass burning emission inventories.**

	Emission factors across inventories and vegetation types (g species per kg dry matter)							
Types	CO				OC			
	FINN1.5	GFED4s	QFED2.5	VFEI0	FINN1.5	GFED4s	QFED2.5	VFEI0
Temperate forest	108[Ak]	88[Ak]	107[AM]	113[An]	6.97[AR]	9.6[AM]	41.09*	10.9[An]
Boreal forest	118[Ak]	127[Ak]	107[AM]	121[An]	7.31[Mc]	9.6[AM]	41.09*	5.9.[An]
Savanna and Grass, shrub	59[Ak]/68[Ak]	63[Ak]	65[AM]	69[An]	2.6[Ak]/6.61[Mc]	2.62[Ak]	6.12*	3[An]
Tropical forest	92[Ak]	93[Ak]	104[AM]	104[An]	4.77[Ak]	4.71[Ak]	13*	4.4[An]
Agricultural	111[Ak]	102[Ak]	/	76[An]	3.3[AM]	2.3[Ak]	/	4.9[An]
Peatlands	/	210[#]	/	260[An]	/	6.02[#]	/	14.2[An]

1121   Ak: Akagi et al. (2011);   AM: Andreae and Merlet (2001);   An: Andreae (2019);   AR: Andreae and Rosenfeld (2008);   Mc: McMeeking et al. (2009)

1122   *: QFED2.5 PM-related emission factors are obtained by multiplying the base EF multiplied by its biome-specific enhancement factor

1123   #: Emission factors for peatland is the average of lab measurements of Yokelson et al. (1997) and Christian et al. (2003)

1124

1125

1126 **Table 3. Comparison of CESM-CAM6 simulated CO column averages and satellite retrieved CO**
1127 **column averages during the fire season.**

Regions	Fire-Season	Satellite	CESM2-CAM6			
		MOPITT	FINN1.5	GFED4s	QFED2.5	VFEI0
EQAS	Jan.-Apr.	1.88	1.66	*1.69*	1.61	1.47
BONA	Apr.-Aug.	2.03	1.29	*1.47*	1.30	1.32
SEAS	Feb.-Apr.	2.40	*2.10*	1.94	1.89	1.95
SHAF	May.-Nov.	2.31	1.75	2.04	1.99	*2.19*
NHAF	Jan.-May.	2.66	1.96	2.02	2.05	*2.10*
BOAS	Mar.-Nov.	2.05	1.31	*1.42*	1.33	1.34
SHSA	July.-Dec.	1.77	*1.75*	*1.80*	*1.76*	*1.80*

1128

1129

1130   **Table 4. Same as Table 3 but for AOD**

| Regions | Satellite | CESM2-CAM6 | | | |
	MODIS	FINN1.5	GFED4s	QFED2.5	VFEI0
EQAS	0.23	*0.22*	*0.25*	*0.23*	*0.21*
BONA	0.13	0.07	*0.12*	*0.11*	0.07
SEAS	0.30	0.35	*0.30*	0.36	*0.30*
SHAF	0.33	*0.31*	*0.37*	0.53	*0.40*
NHAF	0.32	*0.53*	0.54	0.61	0.55
BOAS	0.15	0.11	*0.13*	*0.16*	0.11
SHSA	0.14	0.30	0.31	0.34	*0.29*

1131

1132

1133

1134

(a) The Fraction of Biomass Burning CO in Total CO

(b) CO emissions from Biomass Burning

BONA: Boreal North America   SHSA: South Hemispheric South America

BOAS: Boreal Asia   SEAS: Southeast Asia and India   EQAS: Equatorial Asia

NHAF: Northern Hemispheric Africa   SHAF: Southern Hemispheric Africa
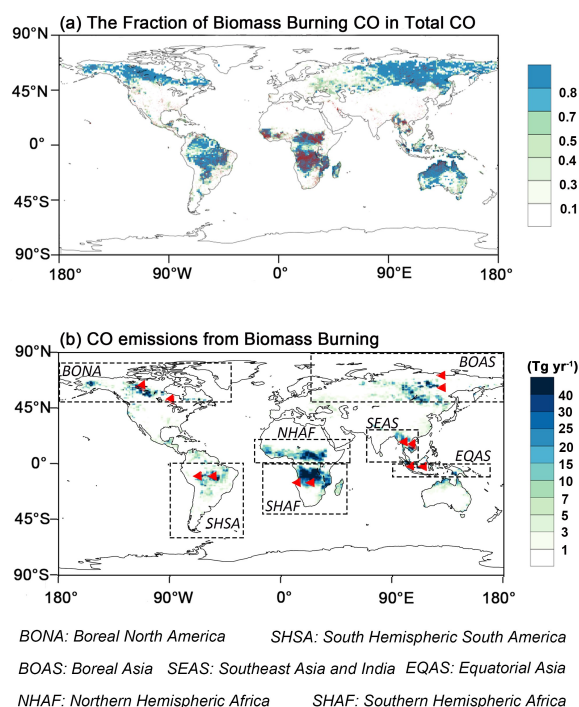
1135

Figure 1. (a) The fraction of BB CO emissions to the sum of anthropogenic and BB CO emissions (CO_BB/CO_Total) during 2013-2016 and (b) the spatial distribution of CO emissions (FINN1.5 was used as an example). The red dots in Fig. 1(a) are the fire points from the MCD14DL satellite product. In Fig. 1(b), seven regions with high BB emissions taken from those applied by van der Werf et al. (2006, 2010) are marked with black boxes, and the red triangles represent 12 AERONET stations. In this study, seven major BB regions includes Boreal North America (BONA), Boreal Asia (BOAS), Southeast Asia (SEAS), Equatorial Asia (EQAS), North Hemisphere Africa (NHAF), South Hemisphere Africa (SHAF), and South Hemisphere South America (SHSA).

1136
1137
1138
1139
1140
1141
1142
1143

1144

1145

1146

32
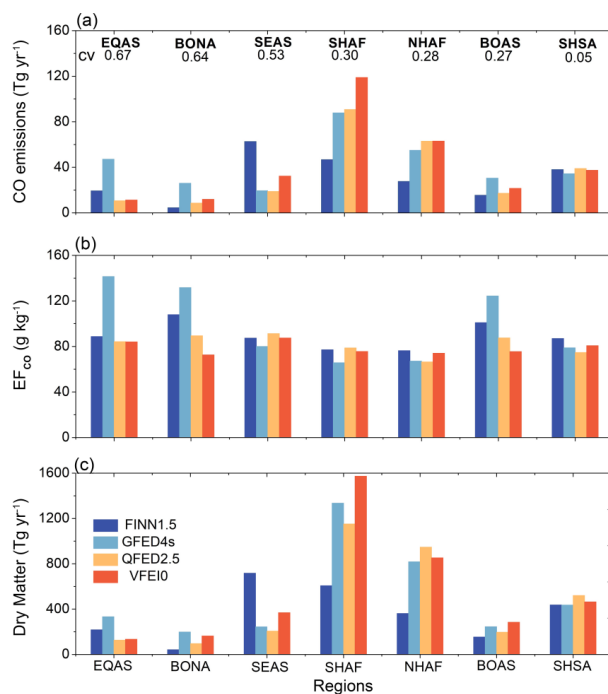
Figure 2. (a) Average annual CO emissions of four biomass burning emission inventories across seven major BB regions during 2013-2016. The cv, defined as the ratio of the standard deviation to the mean, is the coefficient of variation among the emissions of four datasets. (b) and (c) are the same as (a), but for the emission factor of CO (EF_{CO}) and Dry Matter.
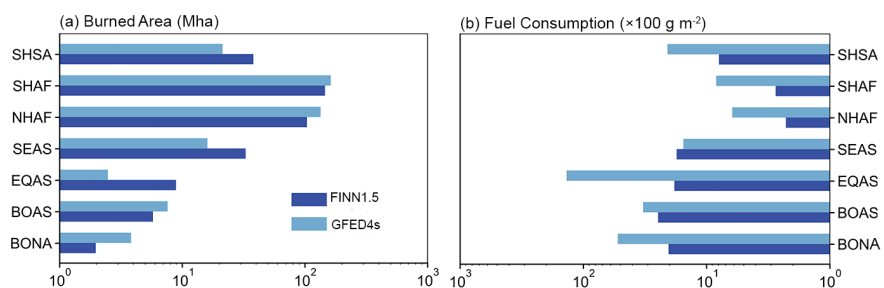
Figure 3. Annual burned area (a) and fuel consumption (b) of two bottom-up datasets (FINN1.5 and GFED4s) across seven regions from 2013 to 2016.

1164
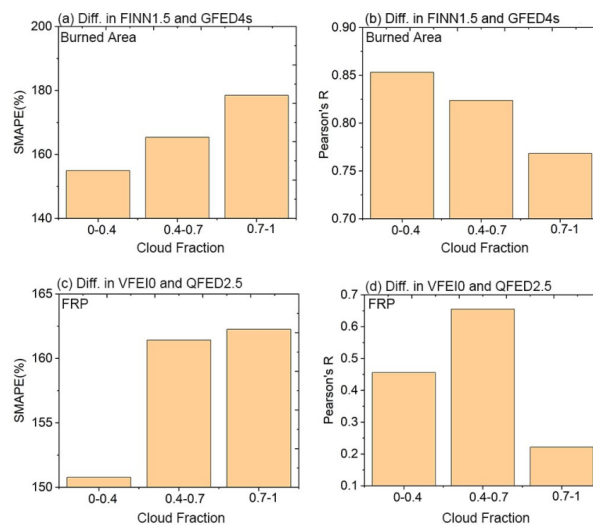
1165

Figure 4. The differences in (a-b) burned areas and (c-d) total FRP detected by two inventories under
different cloud fraction in a pilot region of BONA. These differences are quantified by two indicators:
SMAPE and Pearson's R. Could fraction data is calculated from MODIS product MCD06COSP.

1169

1170
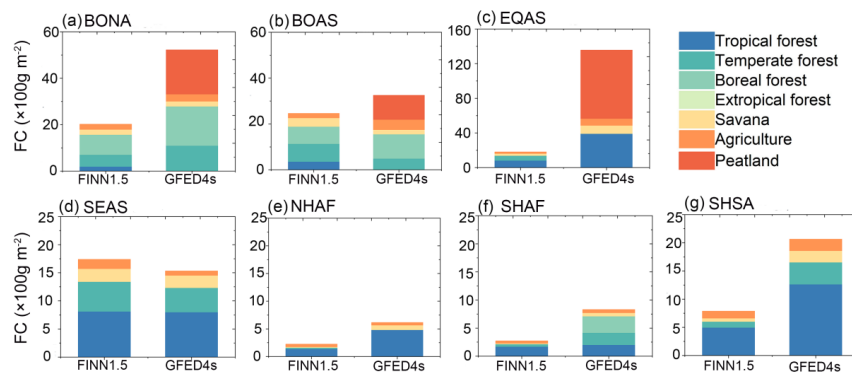
1172

Figure 5. Annual average fuel consumption of two bottom-up datasets (FINN1.5 and GFED4s) across

1174 seven regions from 2013 to 2016. The contributions of the seven biomes are shown in different colors.

1175

1176

1177
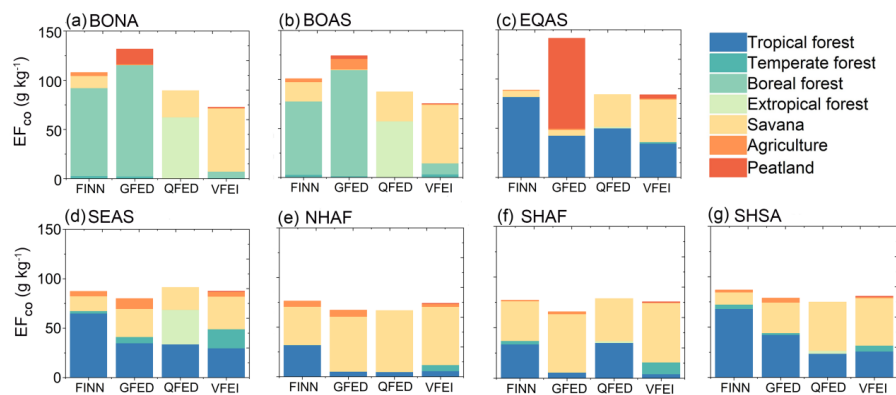
1178

1179 **Figure 6.** Regional comprehensive emission factors for four datasets (FINN1.5, GFED4s, QFED2.5,
1180 and VFEI0) in seven regions from 2013 to 2016. The contributions of the seven biomes are shown in
1181 different colors.

1182

1183

1184
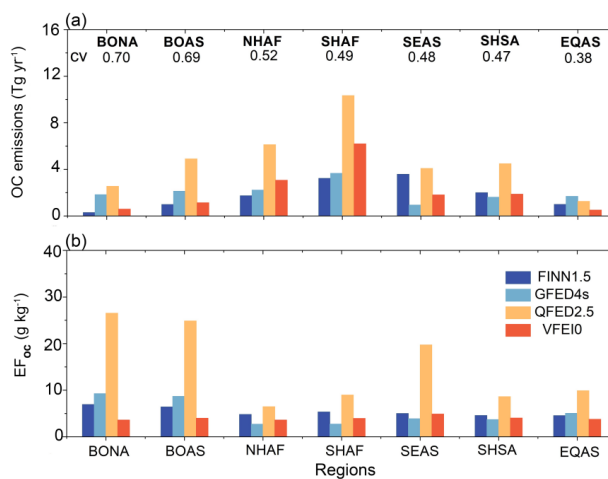
1185

Figure 7. (a) Average annual OC emissions of four biomass burning emissions inventories across seven major BB regions during 2013-2016. The cv, defined as the ratio of the standard deviation to the mean, is the coefficient of variation among the emissions of four datasets. (b) is the same as (a) but for the emission factor of OC (EF_{oc}).

1190
1191

1192
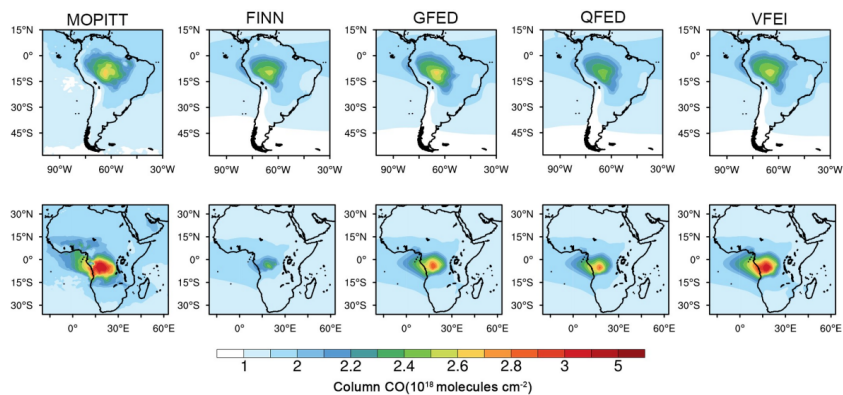
1193

Figure 8. Spatial distribution of CO column burdens from MOPITT and CESM2-CAM6 simulations
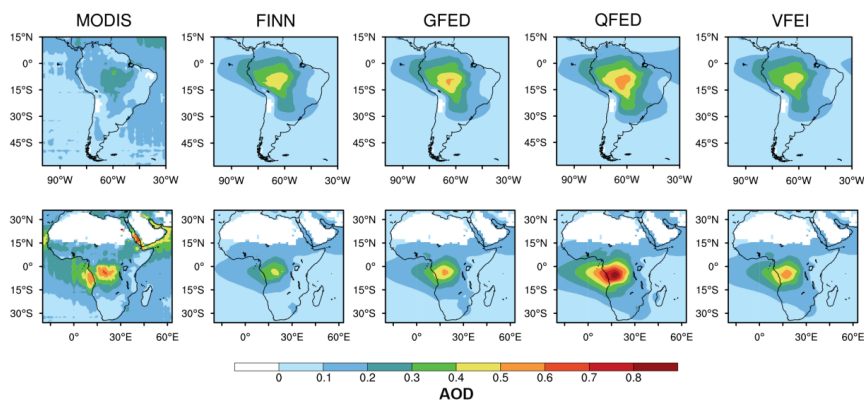during the fire season (Table 3). The text above each plot identifies the name of the satellite inversion
dataset or emission inventory dataset applied by the model, namely FINN1.5, GFED4s, QFED2.5, and
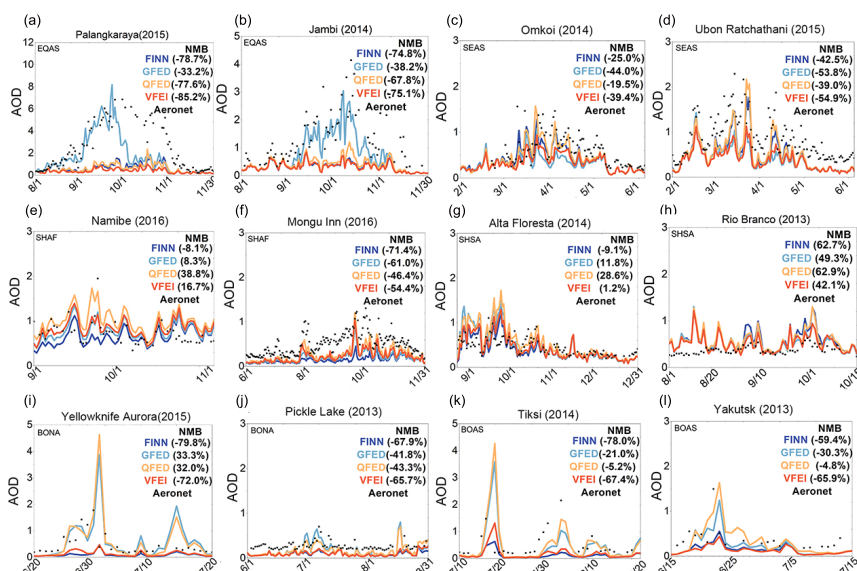VFEI0.

1199

1200

Figure 9. The same as figure 8 but for AOD.

1202

1203

1204

1205

1206 **Figure 10.** Comparison between AOD simulated by CESM2-CAM6 using the four datasets (FINN1.5,
1207 GFED4s, QFED2.5, and VFEI0) and AERONET ground-based observations during fire seasons. These
1208 AERONET sites are: (a) Palangkaraya (2.2°S, 113.9°E), (b) Jambi (1.6°S, 103.6°E), (c) Omkoi (17.8°N,
1209 98.4°E), (d) Ubon Ratchathani (15.2°N, 104.9°E), (e) Namibe (15.2°S, 12.2°E), (f) Mongu Inn (15.3°S,
1210 23.1°E), (g) Alta Floresta (9.9°S, 56.1°W), (h) Rio Branco (9.9°S, 67.9°W), (i) Yellowknife_Aurora
1211 (62.5°N, 114.4°W), (j) Pickle Lake (51.4°N, 90.2°W), (k) Tiksi (71.6°N, 128.9°E), (l) Yakutsk (61.7°N,
1212 129.4°E).

1213